

# Evidence for a Rotational Component in the CGM of Nearby Galaxies\*

DAVID M. FRENCH<sup>1,2</sup> AND BART P. WAKKER<sup>2</sup>

<sup>1</sup>*Space Telescope Science Institute, 3700 San Martin Drive, Baltimore, MD 21218*

<sup>2</sup>*Department of Astronomy, University of Wisconsin, Madison, WI 53706, USA*

## ABSTRACT

We present results of a study comparing the line-of-sight velocity of Ly $\alpha$  absorbers relative to the rotation velocity of nearby galaxy disks in the local Universe ( $z \leq 0.03$ ). We have obtained rotation curves via long-slit spectroscopy of 8 galaxies with the Southern African Large Telescope, and combine this dataset with an additional 16 galaxies with published rotation curves from the literature. Each galaxy appears within  $3R_{\text{vir}}$  of a QSO sightline with available Cosmic Origin Spectrograph (COS) data covering the relevant Ly $\alpha$  wavelength range. We study the on-sky velocity orientation of absorbers with respect to nearby galaxy rotation, and compare with results from both the Steidel et al. (2002) monolithic halo model and a new NFW galaxy halo rotation model to interpret these data in the context of probing three-dimensional galaxy halos via 1-dimensional QSO absorption-line spectroscopy. Relative to these model we find that up to 59% of Ly $\alpha$  absorbers have velocities consistent with co-rotation. Intriguingly, we find the Ly $\alpha$  co-rotation fraction to decrease with galaxy luminosity ( $L^*$ ) and impact parameter in a model independent fashion. We report that both anti-rotating absorbers and those found near luminous galaxies ( $L \gtrsim 0.5L^*$ ) mostly have low Doppler  $b$ -parameters ( $b \lesssim 50 \text{ km s}^{-1}$ ). Absorbers consistent with co-rotation show a wide range of Doppler  $b$ -parameters. These results are broadly in agreement with the co-rotation fractions predicted by simulations, and furthermore are consistent with the cold- and hot-mode accretion regimes predicted to occur in the low- $z$  Universe. Finally, we find a strong anti-correlation between co-rotation fraction and galaxy inclination, which is at odds with recent metal-line kinematic studies and suggests the kinematic and geometric distribution of the circumgalactic medium is complex and multi-phase.

*Keywords:* galaxies:intergalactic medium, galaxies:evolution, galaxies:halos, quasars: absorption lines

## 1. INTRODUCTION

Our current Lambda Cold-Dark-Matter ( $\Lambda$ CDM) cosmology picture describes galaxies forming hierarchically out of overdensities in the underlying dark matter distribution. As the surrounding intergalactic medium (IGM) is funneled toward a growing galaxy, simulations predict the angular momentum of the inflowing gas is redistributed onto the disk and seeds the overall rotation of the galaxy (e.g., Chen et al. 2003; Sharma & Steinmetz 2005; Brook et al. 2011; Kimm et al. 2011; Pichon et al. 2011; Stewart et al. 2011a, 2013; Ho et al. 2019). As this infalling gas is responsible for birthing and continuing to feed the galaxies throughout their lifetimes, it is expected that the extended gaseous halos should rotate in the same sense as both the galactic disks and dark matter halos.

In this  $\Lambda$ CDM picture, accretion falls broadly into two types. In the so-called “hot-mode”, gas shock-heats at the virial radius as it encounters the galaxy halo. The

inner, more dense region of this hot gaseous halo then rains down onto the disk as it radiatively cools (e.g., Fillmore & Goldreich 1984; Bertschinger 1985; Danovich et al. 2012; Shen et al. 2013; Stevens et al. 2017). However, most gas arrives cold ( $T \sim 10^4 \text{ K}$ ) from the IGM, and the proposed radiative shock is unstable to cooling. Thus this hot-halo scenario may not actually be created (Birnbom & Dekel 2003; Kereš et al. 2005; Ocvirk et al. 2008; Brooks et al. 2009; Dekel et al. 2009).

In contrast, as part of the alternative “cold-mode” accretion model, filaments of gas from the IGM would merge smoothly with the disk, thus converting a significant fraction of their infall velocity to rotational velocity of the galaxy (Kereš et al. 2005; Stewart et al. 2017; El-Badry et al. 2018). The simulations of Powell et al. (2011) agreed with these conjectures by showing that indeed, the accreting filaments connect rather smoothly to the disc, even in the presence of strong supernova driven winds. This cold-mode of accretion likely dominates the global growth of all but the most massive halos at high redshifts ( $z \gtrsim 3$ ), and the growth of lower mass ( $M_{\text{halo}} \leq 5 \times 10^{11} M_*$ ) objects at late times (Dekel & Birnbom 2006; van de Voort et al. 2011). Furthermore, cosmological SPH simulations such as those by Stewart

\* Based on observations made with the Southern African Large Telescope (SALT).

et al. (2011b, 2013); Ho et al. (2019) suggests that halo gas should co-rotate with disk-gas out to at least 100 kpc, and that absorption in intervening QSO sightlines should be able to accurately capture this rotation signature. Thus, observing co-rotating gas in the halos of galaxies would provide the most direct evidence of cold-mode accretion.

Some observational evidence of co-rotating halo gas has been obtained at higher redshifts. In pioneering studies focusing on the Mg II absorber kinematics and their connection with neighboring galaxies, Charlton & Churchill (1998) and Steidel et al. (2002) (and later Kacprzak et al. 2010; Bouché et al. 2013, 2016; Ho et al. 2017; Martin et al. 2019, see also Kacprzak 2017 for a review) found tantalizing evidence that a significant fraction of Mg II absorbers have velocities that can be explained by an extended gaseous disk. Approaching the question from a different angle, Bowen et al. (2016) probed the halo of a single galaxy, NGC1097, with 4 nearby QSO sightlines, and suggests that an extended, slowly rotating disk with additional inflowing IGM material best matches observations. Additionally, Diamond-Stanic et al. (2016) detect co-rotating H $\alpha$  emission and Mg II and Fe II absorption toward a Milky Way-like galaxy at  $z = 0.413$ .

However, as noted by Steidel et al. (2002) among others, a simple extended disk model is insufficient to explain the observed bulk motion implied by their sample of 5 Mg II absorber-galaxy systems, and a rotating *halo* may be a better model.

Additionally, the picture may have changed since  $z \sim 0.5$ , the epoch 5 Gyr ago that most of these Mg II systems are probing. By  $z \sim 0$  simulations (e.g., Kereš et al. 2005; Stewart et al. 2017) predict a drop-off in cold-mode accretion and a decrease in the density of IGM filaments. Observational confirmation has been even more inconclusive in this low-redshift regime. In the largest such study, involving Ly $\alpha$  absorber-galaxy kinematics, Côté et al. (2005) probed the halos of nine galaxies using *HST* observed background QSOs, and found that large warps would be needed to explain the velocity of H I absorbers by an extended rotating disk. Additionally, Wakker & Savage (2009) compiled a sample of 76 sightlines, which included only 4 galaxy-QSO systems for which the galaxy’s rotation curve was known from the literature, and found only 1/4 of Ly $\alpha$  absorbers appeared to co-rotate with the associated galaxy disk. Similarly, Kacprzak et al. (2011) claim a reduction in Mg II co-rotation around  $\sim L^*$  galaxies between  $z \sim 0.5$  and  $z \sim 0.1$ .

This current work aims to address many of these observational challenges. Firstly, by significantly increasing the sample size of galaxy-absorber systems, and secondly, by implementing a 3-dimensional rotating halo model to aid in the interpretation challenge inherent in a 1D sightline probing a 3D structure. To significantly improve observational statistics in this low-redshift regime, we

have obtained rotation curves from the Southern African Large Telescope (SALT) for 8 nearby spiral galaxies which are located within  $3R_{\text{vir}}$  of a background QSO observed by the Cosmic Origins Spectrograph (COS) on *HST*. A literature search yielded an additional 16 galaxies with published rotation curves and known orientations. Each of these is probed by at least one QSO within  $3R_{\text{vir}}$ .

In Section 2 we describe the selection and reduction of both SALT and COS spectra. In Section 3 we present the rotating halo model we have developed to aid in the interpretation of our observations. In Section 4 we discuss the overall results of this exercise and present a physically-motivated interpretation of these results. See Section 5 for a summary of our results and conclusions. Each galaxy-QSO system is discussed in detail in Appendix A (SALT-observed galaxies) and B (galaxies from the literature).

## 2. DATA AND ANALYSIS

### 2.1. SALT Data

Our sample contains 8 galaxies observed with the Southern African Large Telescope (SALT) Robert Stobie Spectrograph (RSS) in longslit mode (Burgh et al. 2003; Kobulnicky et al. 2003; Buckley et al. 2006; O’Donoghue et al. 2006). Our selection of these galaxies and associated QSO targets included several steps. First we identified galaxies in the NASA Extragalactic Database (NED) that are visible to SALT, within the redshift window of  $z \leq 0.33$  ( $cz \leq 10,000 \text{ km s}^{-1}$ ), and within  $3R_{\text{vir}}$  of QSOs with existing COS G130M spectra available. From these we selected those with angular sizes less than  $6'$  to enable easy sky subtraction using the outer edges of the slit and thus avoiding additional, off-target exposures, and surface brightnesses sufficient to keep exposure times below  $\sim 1300\text{s}$ . This resulted in a pool of 48 galaxies, which were submitted to the SALT observing queue with the expectation that SALT would observe as many as possible within our awarded time. We obtained data for 14 galaxies, but 2 proved to be unusable due to issues with spectral identification and low signal-to noise.

Finally, we applied the QSO-galaxy matching scheme outlined in French & Wakker (2017) to exclude systems for which multiple galaxies could reasonably be matched with a particular absorption line. In short, for each QSO-galaxy system we calculate the likelihood value  $\mathcal{L} = e^{-(\rho/R_{\text{vir}})^2} e^{-(\Delta v/200)^2}$ , where  $\rho$  is the impact parameter,  $R_{\text{vir}}$  the galaxy virial radius and  $\Delta v$  the difference between the absorption and galaxy system velocities. We require that  $\mathcal{L} \geq 0.01$  for all systems, and for no other nearby galaxies to be within a factor of  $5\mathcal{L}$ . This requires that the QSO be within approximately  $3R_{\text{vir}}$  of the galaxy, and be obviously closer than any other neighboring galaxies. After a careful inspection using this scheme we chose to remove an additional 4 galaxies from the SALT sample.

**Table 1.** SALT Galaxy Observations

Galaxy	R.A.	Dec.	$v_{\text{sys}}$	Published $v_{\text{sys}}$	Type	$v_{\text{obs}}$	$v_{\text{rot}} = v_{\text{obs}}/\sin(i)$	Obs. Date	$T_{\text{exp}}$
			(km s <sup>-1</sup> )	(km s <sup>-1</sup> )		(km s <sup>-1</sup> )	(km s <sup>-1</sup> )		(ks)
(1)	(2)	(3)	(4)	(5)	(6)	(7)	(8)	(9)	(10)
CGCG039-137	11 21 27.0	+03 26 41.7	6918 ± 24	6902 ± 52 <sup>a</sup>	Scd	132 ± 16	143 ± 25	05 11 2016	700
ESO343-G014	21 37 45.2	-38 29 33.2	9139 ± 32	9162 ± 45 <sup>b</sup>	S	203 ± 32	203 ± 32	05 16 2016	1000
IC5325	23 28 43.4	-41 20 00.5	1512 ± 8	1503 ± 7 <sup>c</sup>	SAB(rs)bc	53 ± 5	125 ± 27	05 17 2016	600
MCG-03-58-009	22 53 40.9	-17 28 44.0	9015 ± 19	9030 ± 10 <sup>d</sup>	Sc	150 ± 11	171 ± 22	05 16 2016	1200
NGC3633	11 20 26.2	+03 35 08.2	2587 ± 7	2600 ± 2 <sup>f</sup>	SAa	149 ± 6	157 ± 9	05 11 2016	1200
NGC4939	13 04 14.4	-10 20 22.6	3093 ± 33	3110 ± 4 <sup>e</sup>	SA(s)bc	204 ± 23	234 ± 39	05 14 2016	500
NGC5786	14 58 56.3	-42 00 48.1	2975 ± 22	2998 ± 5 <sup>h</sup>	SAB(s)bc	156 ± 14	172 ± 25	05 11 2016	250
UGC09760	15 12 02.4	+01 41 55.5	2094 ± 16	2023 ± 2 <sup>i</sup>	Sd	46 ± 10	46 ± 16	05 11 2016	500

NOTE—SALT targeted galaxies. Columns are as follows: 1) the galaxy name, 2), 3) R.A., Dec. in J2000, 4) measured galaxy systemic velocity, 5) published galaxy systemic velocity, 6) morphological type (RC3), 7) observed rotation velocity, 8) inclination-corrected rotation velocity, 9) observation date, and 10) exposure time. All observations used the RSS PG2300 grating.

**References**—a. Abazajian et al. (2005); b. Jones et al. (2009); c. Corwin et al. (1994); d. Mathewson & Ford (1996); e. Koribalski et al. (2004); f. Lu et al. (1993); g. Grogan et al. (1998); h. di Nella et al. (1996); i. Giovanelli et al. (1997)

**Table 2.** Summary of QSO Sample

Target	Galaxy	R.A.	Dec.	z	Program	<sup>a</sup> $T_{\text{exp}}$ (ks)
(1)	(2)	(3)	(4)	(5)	(6)	(7)
2E1530+1511	NGC5951	15 33 14.3	+15 01 03.0	0.09000	14071	9348
3C232	NGC3067	09 58 20.9	+32 24 02.0	0.53060	8596	44662
CSO295	NGC3432	10 52 05.6	+36 40 40.0	0.60900	14772	1088
FBQSJ0908+3246	NGC2770	09 08 38.8	+32 46 20.0	0.25989	14240	7430
MRC2251-178	MCG-03-58-009	22 54 05.9	-17 34 55.0	0.06609	12029	5515
MRK335	NGC7817	00 06 19.5	+20 12 11.0	0.02578	11524	5122
MRK771	NGC4529	12 32 03.6	+20 09 30.0	0.06301	12569	1868
MRK876	NGC6140	16 13 57.2	+65 43 11.0	0.12900	11524	12579
PG0804+761	UGC04238	08 10 58.7	+76 02 43.0	0.10200	11686	5510
PG1259+593	UGC08146	13 01 12.9	+59 02 07.0	0.47780	11541	9200
PG1302-102	NGC4939	13 05 33.0	-10 33 19.0	0.27840	12038	5979
QSO1500-4140	NGC5786	15 03 34.0	-41 52 23.0	0.33500	11659	9258
RBS1503	NGC5907	15 29 07.5	+56 16 07.0	0.09900	12276	1964
RBS1768	ESO343-G014	21 38 49.9	-38 28 40.0	0.18299	12936	6962
RBS2000	IC5325	23 24 44.7	-40 40 49.0	0.17359	13448	5046
RX_J1017.5+4702	NGC3198	10 17 31.0	+47 02 25.0	0.33544	13314	8655
RX_J1054.2+3511	NGC3432	10 54 16.2	+35 11 24.0	0.20300	14772	533
RX_J1117.6+5301	NGC3631	11 17 40.5	+53 01 51.0	0.15871	14240	4943
RX_J1121.2+0326	CGCG039-137, NGC3633	11 21 14.0	+03 25 47.0	0.15200	12248	2695
RX_J1236.0+2641	NGC4565	12 36 04.0	+26 41 36.0	0.20920	12248	4235
SBS1116+523	NGC3631	11 19 47.9	+52 05 53.0	0.35568	14240	4949
SDSSJ091052.80+333008.0	NGC2770	09 10 52.8	+33 30 08.0	0.11631	14240	7442
SDSSJ091127.30+325337.0	NGC2770	09 11 27.3	+32 53 37.0	0.29038	14240	10028
SDSSJ095914.80+320357.0	NGC3067	09 59 14.8	+32 03 57.0	0.56462	12603	2273
SDSSJ104335.90+115129.0	NGC3351	10 43 35.9	+11 05 29.0	0.79400	14071	4736
SDSSJ111443.70+525834.0	NGC3631	11 14 43.7	+52 58 34.0	0.07921	14240	13440
SDSSJ112439.50+113117.0	NGC3666	11 24 39.4	+11 31 17.0	0.14300	14071	10427
SDSSJ112448.30+531818.0	UGC06446, NGC3631	11 24 48.3	+53 18 19.0	0.53151	14240	7920
SDSSJ151237.15+012846.0	UGC09760	15 12 37.2	+01 28 46.0	0.26625	12603	7590
TON1009	NGC2770	09 09 06.2	+32 36 30.0	0.81028	12603	4740
TON1015	NGC2770	09 10 37.0	+33 29 24.0	0.35400	14240	4774

All SALT galaxy spectra were reduced and extracted using the standard PySALT reduction package (Crawford et al. 2010)<sup>1</sup>, which includes procedures to prepare the data, correct for gain, cross-talk, bias, and overscan, and finally mosaic the images from the 3 CCDs. Next, we rectify the images with wavelength solutions found via Ne and Ar arc lamp spectra. Finally, we perform a basic sky subtraction using an off-target portion of the spectrum, and extract 5-10 pixel wide 1-D strips from the reduced 2-D spectrum.

For each resulting 1-D spectrum, we identify the H $\alpha$  emission lines and perform a non-linear least-squares Voigt profile fit using the Python package LMFIT<sup>2</sup>. While normally Gaussian profiles are used for fitting emission lines, we found a Voigt profile resulted in a better fit of the peak velocity (which is the measurement of prime importance for this analysis). The line centroid and  $1\sigma$  standard errors are returned, and these fits are then shifted to rest-velocity based on the galaxy systemic redshift with heliocentric velocity corrections calculated via the IRAF *rvcorrect* procedure. The final rotation velocity is calculated by then applying the inclination correction,  $v_{\text{rot}} = v / \sin(i)$ .

Final errors are calculated as a quadrature sum of  $1\sigma$  fit errors, systemic redshift error, and inclination uncertainty as follows:

$$\sigma^2 = \left( \frac{\partial v_{\text{rot}}}{\partial \lambda_{\text{obs}}} \right)^2 (\Delta \lambda_{\text{obs}})^2 + \left( \frac{\partial v_{\text{rot}}}{\partial v_{\text{sys}}} \right)^2 (\Delta v_{\text{sys}})^2 + \left( \frac{\partial v_{\text{rot}}}{\partial i} \right)^2 (\Delta i)^2, \quad (1)$$

where  $\Delta \lambda_{\text{obs}}$ ,  $\Delta v_{\text{sys}}$ , and  $\Delta i$  are the errors in observed line center, galaxy redshift, and inclination, respectively. We determine the inclination error by calculating the standard deviation of the set of all axis ratio values available in NED for each galaxy. This inclination component tends to dominate the error for low-inclination galaxies.

The final physical scale is calculated using the SALT image scale of 0.1267 arcsec/pixel, multiplied by the 4-pixel spatial binning, and converted to physical units using a redshift-independent distance if available, and a Hubble flow estimate if not (corrected for Virgocentric flow following Huchra & Geller (1982)). We adopt a Hubble constant of  $H_0 = 71 \text{ km s}^{-1} \text{ Mpc}^{-1}$  throughout.

Finally, we calculate our approaching and receding velocities via a weighted mean of the outer 1/2 of each rotation curve, with errors calculated as weighted standard errors in the mean. Our final redshifts are calculated

by forcing symmetric rotation, such that the outer 1/2 average velocity for each side matches in magnitude. The upper-left panel of Figure 1 shows an example of this; the black points and error bars are the observed rotation measurements, the dark green lines show the average rotation velocity for the outer 1/2 edge of each rotation curve, and the green shading shows the  $1\sigma$  error for this average value. Table 1 summarizes the observations for this final sample. See Appendix A for rotation curves and finder charts for each observed galaxy.

## 2.2. Additional Galaxy Data

We have augmented our observed sample of galaxies with an additional 16 systems from the literature. While rotation curves for many galaxies have been published, a far smaller sample also included the necessary orientation information for our purposes. Of these, only the 18 included here were also relatively isolated based on our likelihood criteria and within  $3R_{\text{vir}}$  of a background QSO with sufficient spectral coverage and signal-to-noise. The resulting sample come from a variety of sources, and we have endeavored to keep the galaxy properties (e.g.,  $i$ ,  $v_{\text{sys}}$ ) adopted by the original data authors. For a small subset of these we have adopted more modern inclination and/or position angle measurements where appropriate (see Appendix B for details). We used the plot digitization software WebPlotDigitizer<sup>3</sup> to extract rotation curve data from figures when necessary. Rotation velocity errors are calculated with Eq. 1 as for the SALT observed sample.

## 2.3. COS Spectra

The Barbara A. Mikulski Archive for Space Telescopes (MAST) archives yield 31 QSO targets observed by COS which lie within  $3R_{\text{vir}}$  of our SALT galaxies. These targets vary widely in signal-to-noise from approximately 5 to 100 due to our choosing them based only on their proximity to galaxies with known rotation. The reduction procedure for these spectra follow those described by Wakker et al. (2015) and French & Wakker (2017). In short, spectra are processed with CALCOS v3.0 or higher and are aligned using a cross-correlation, and then shifted to make sure that (a) the velocities of the interstellar lines match the 21-cm HI profile, and (b) the velocities of lines in a single absorption system line up properly. Multiple exposures are combined by summing total counts per pixel before converting to flux. The COS instrument is described in detail by Green et al. (2012).

Once reduced we fit each absorption system with Voigt profiles using the VoigtFit package (Krogager 2018). The VoigtFit routine first fits a continuum around the line region using third-order or lower Chebyshev polynomials. Instrumental broadening is taken into account by convolving COS line-spread function (LSF) tables for

<sup>1</sup> <http://pysalt.salt.ac.za/>

<sup>2</sup> <http://cars9.uchicago.edu/software/python/lmfit/contents.html>

<sup>3</sup> WebPlotDigitizer; <http://arohatgi.info/WebPlotDigitizer>



the appropriate central wavelength and detector lifetime position with the fitted Voigt profile model. In all cases we use the minimum number of components to obtain a satisfactory fit (i.e., reduced  $\chi^2 \sim 1$ ). The resulting component velocities  $v$ , column densities  $N$ , Doppler widths  $b$  and associated errors are reported in Table 3.

### 3. HALO ROTATION MODEL

In order to better understand how the potential 3D rotation of galaxy halo gas is mapped onto a one-dimensional QSO sightline, we have developed a simple halo rotation model. This model is seeded by an observed rotation curve, which is then extrapolated out to a radius and height of  $3R_{\text{vir}}$  to form a coherently rotating cylindrical halo. For each galaxy-QSO pair we create 2 rotation models: 1) a model with rotation velocities which smoothly decline as a function of radius based on a Navarro-Frenk-White (NFW) profile fit (Navarro et al. 1996, 1997) to the rotation curve data, and 2) the thick-disk model developed in Steidel et al. (2002). The results of these models will also be compared with using the simple on-sky apparent velocity of each galaxy below.

For our cylindrical model, we first fit a NFW rotation velocity profile to the observed rotation curve. The form of this NFW fit is as follows:

$$V(R) = V_{200} \left[ \frac{\ln(1+cx) - cx/(1+cx)}{x[\ln(1+c) - c/(1+c)]} \right]^{\frac{1}{2}}, \quad (2)$$

where  $x = R/R_{200}$ , with  $R_{200}$  being the radius at which the density contrast with respect to the critical density of the universe exceeds 200,  $c = R_{200}/R_s$ , with  $R_s$  being the characteristic radius of the halo, and  $V_{200}$  being the characteristic velocity at  $R_{200}$ . For all fits  $R_{200}$  is set to each galaxy's virial radius,  $R_{\text{vir}}$ . We have taken this form from de Blok et al. (2008). The resulting NFW fits tend to be somewhat poor toward the inner parts of the rotation curve (as has been noted by others, e.g., Côté et al. 2005). Regardless, we are most interested in achieving a physically-motivated, declining velocity profile in the outer halo regions where most of our QSO sightlines are located, for which these fits are certainly adequate.

We estimate the virial radius of each galaxy according to the combined "halo-matching" and constant mass-to-light ratio technique developed in Stocke et al. (2013) (see the green line in their Figure 1). This method uses a halo matching with the CfA B-band galaxy luminosity

function of Marzke et al. (1994) with  $\alpha = 1.25$  for the faint  $L < 0.2L^*$  end of the luminosity function, and a constant mass-to-light ratio of  $M_{\text{halo}}/L_{\text{gal}} = 50M_{\odot}/L_{\odot}$  above this (see Stocke et al. 2013 and references therein for further detail).

Next, we project the NFW fit onto a plane oriented to a mock QSO sightline identically to the input galaxy-QSO pair orientation. By then stacking multiple such rotation-planes along the galaxy z-axis direction, we build a cylindrical halo embedded with the rotation curve fit.

Finally, we calculate the projected rotation velocity encountered at each position along the sightline. The result is a function representing the rotation velocity encountered by the sightline as a function of distance along it. Hence, each model produces the velocity a co-rotating absorber would project onto the spectrum as a function of distance from the center of the galaxy (scaled according to  $R_{\text{vir}}$ ).

Finally, we also compute the co-rotation velocity ranges produced by the thick-disk model developed by Steidel et al. (2002). This model produces a line-of-sight velocity  $v_{\text{los}}$  as a function of impact parameter  $\rho$ , galaxy inclination  $i$ , QSO-galaxy azimuth angle  $\Phi$ , and maximum projected rotation velocity  $v_{\text{max}}$  as follows:

$$v_{\text{los}} = \frac{-v_{\text{max}}}{\sqrt{1 + \left(\frac{y}{p}\right)^2}} e^{-\frac{|y-y_0|}{h_v \tan i}} \text{ with,} \\ y_0 = \frac{\rho \sin \phi}{\cos i} \text{ and } p = \rho \cos \phi. \quad (3)$$

Here  $h_v$  represents the scale height for the velocity lag in the z-direction. We have assumed a thick disk for maximum disk/halo rotation for all galaxies ( $h_v = 1000$  kpc).

We calculate  $1\sigma$  model errors via a bootstrapping method which reruns the NFW fitting and modeling while resampling the rotation curve data points together with a 3 degree position angle uncertainty. The final model output is a minimum and maximum velocity an absorber would need in order to be consistent with co-rotation within these  $1\sigma$  error regions.

Figures 1 illustrates an example model for the SALT-observed galaxy NGC3633, with our observed rotation curve, the NFW fit, and the resulting NFW and Steidel model output velocity distributions from left-to-right on top, and a 3-D halo mockup from 3 different viewing angles on the bottom. In most cases, and as seen in this example, the two model outputs have similar *shape*, but vary in maximum predicted velocity.

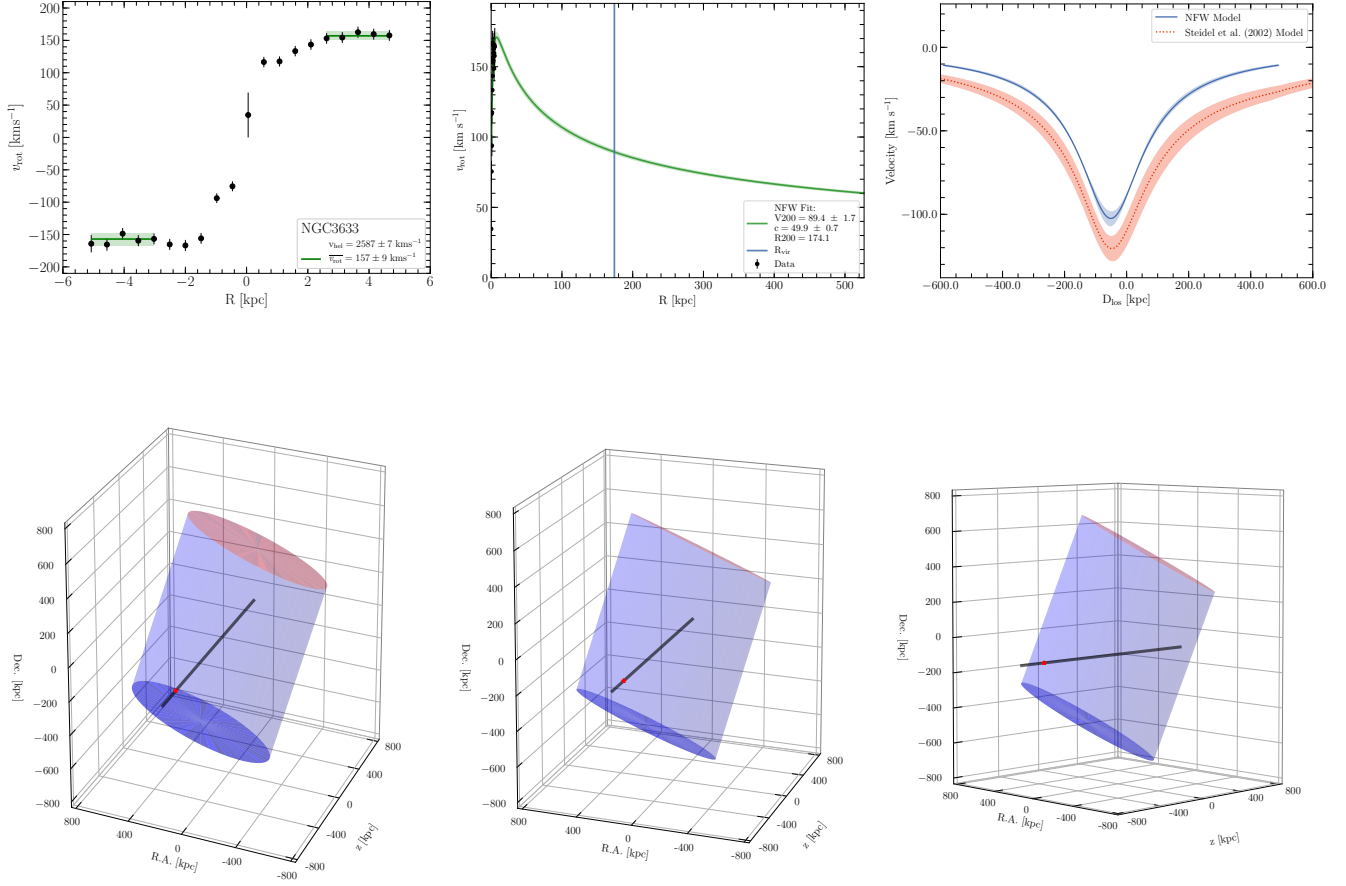


**Figure 1. Top:** Left: The rotation curve for NGC3633 is shown in black, with the outer 1/2 mean rotation velocity indicated in green. Our cylindrical model simply extends this green average velocity out to  $3R_{\text{vir}}$ . Middle: The observed rotation curve is again shown in black, with an NFW profile fit overlaid in green extending to  $3R_{\text{vir}}$  ( $1R_{\text{vir}}$  is shown by the vertical blue line). Right: The resulting model velocity predictions for the cylindrical and NFW models are shown in dashed-black and solid-green (respectively) as a function of velocity along the sightline. **Bottom:** A 3D example mockup of our halo rotation model showing the orientation and extent of the NGC3633 model from 3 different viewing angles. The approaching extreme edge of the NGC3633 cylindrical halo is shown by dark-blue oval, with the far edge shown in red. The black line shows the location of the sightline toward RX\_J1121.2+0326 as it penetrates the halo, with a red star marking the first intercept point.

**Table 3.** Halo Model Results and Ly $\alpha$  Absorption Properties

#	Galaxy	Target	$\rho$ (kpc)	Az. (deg)	Inc. (deg)	$R_{vir}$ (kpc)	$L$ $L_*$	$v_{sys}$ (km s $^{-1}$ )	$v_{rot}^a$ (km s $^{-1}$ )	$\Delta v_{Ly\alpha}$ (km s $^{-1}$ )	$b$ (km s $^{-1}$ )	$\log N$	$v_{Steidel}^b$ (km s $^{-1}$ )	$v_{NFW}^c$ (km s $^{-1}$ )
(1)	(2)	(3)	(4)	(5)	(6)	(7)	(8)	(9)	(10)	(11)	(12)	(13)	(14)	(15)
1	CGCG039-137	RXJ1121.2+0326	99	86	72	155	0.6	6918 $\pm$ 24	136 $\pm$ 24	53 $\pm$ 27	112.2 $\pm$ 17.3	14.27 $\pm$ 0.06	[1.1, 137.2]	[1.6, 210.4]
2	ESO343-G014	RBS1768	466	75	90	187	1.1	9139 $\pm$ 32	-203 $\pm$ 32	166 $\pm$ 32	14.4 $\pm$ 5.9	13.05 $\pm$ 0.08	[-0.1, -0.0]	[-158.8, -20.2]
2	ESO343-G014	RBS1768	466	75	90	187	1.1	9139 $\pm$ 32	-203 $\pm$ 32	244 $\pm$ 32	31.6 $\pm$ 2.9	14.26 $\pm$ 0.03	[-0.1, -0.0]	[-158.8, -20.2]
2	ESO343-G014	RBS1768	466	75	90	187	1.1	9139 $\pm$ 32	-203 $\pm$ 32	308 $\pm$ 32	15.3 $\pm$ 3.5	13.58 $\pm$ 0.06	[-0.1, -0.0]	[-158.8, -20.2]
3	IC5325	RBS2000	314	67	25	175	0.9	1512 $\pm$ 8	-53 $\pm$ 11	84 $\pm$ 9	20.9 $\pm$ 9.0	12.85 $\pm$ 0.1	[-14.6, -1.7]	[-30.3, -4.5]
4	MCG-03-58-009	MRC2251-178	355	74	61	259	2.9	9015 $\pm$ 19	150 $\pm$ 19	14 $\pm$ 19	48.7 $\pm$ 4.9	13.08 $\pm$ 0.04	[15.9, 101.6]	[8.8, 137.4]
5	NGC2770	FBQSJ0908+3246	204	56	80	221	1.8	1948 $\pm$ 4	-146 $\pm$ 6	-38 $\pm$ 5	22.7 $\pm$ 5.0	13.95 $\pm$ 0.1	[-12.2, -3.8]	[-164.9, -14.7]
5	NGC2770	FBQSJ0908+3246	204	56	80	221	1.8	1948 $\pm$ 4	-146 $\pm$ 6	43 $\pm$ 6	37.8 $\pm$ 7.1	13.81 $\pm$ 0.05	[-12.2, -3.8]	[-164.9, -14.7]
6	NGC2770	TON1009	267	38	80	221	1.8	1948 $\pm$ 4	-146 $\pm$ 6	-35 $\pm$ 7	26.0 $\pm$ 10.1	13.38 $\pm$ 0.12	[-23.4, -7.5]	[-142.0, -28.2]
6	NGC2770	TON1009	267	38	80	221	1.8	1948 $\pm$ 4	-146 $\pm$ 6	32 $\pm$ 5	24.5 $\pm$ 3.7	14.06 $\pm$ 0.05	[-23.4, -7.5]	[-142.0, -28.2]
7	NGC2770	TON1015	218	58	80	221	1.8	1948 $\pm$ 4	146 $\pm$ 6	-114 $\pm$ 4	28.3 $\pm$ 2.5	13.96 $\pm$ 0.04	[17.3, 123.8]	[14.3, 163.8]
7	NGC2770	TON1015	218	58	80	221	1.8	1948 $\pm$ 4	146 $\pm$ 6	36 $\pm$ 6	29.6 $\pm$ 8.8	13.24 $\pm$ 0.08	[17.3, 123.8]	[14.3, 163.8]
8	NGC2770	SDSSJ091052.80+333008.0	239	63	80	221	1.8	1948 $\pm$ 4	146 $\pm$ 6	-124 $\pm$ 4	31.1 $\pm$ 3.8	14.05 $\pm$ 0.06	[15.2, 120.4]	[12.9, 167.7]
8	NGC2770	SDSSJ091052.80+333008.0	239	63	80	221	1.8	1948 $\pm$ 4	146 $\pm$ 6	21 $\pm$ 6	20.4 $\pm$ 10.2	13.22 $\pm$ 0.11	[15.2, 120.4]	[12.9, 167.7]
9	NGC2770	SDSSJ091127.30+325337.0	234	33	80	221	1.8	1948 $\pm$ 4	-146 $\pm$ 6	114 $\pm$ 11	28.0 $\pm$ 10.0	14.0 $\pm$ 0.2	[-134.2, -35.8]	[-141.9, -27.9]
10	NGC3067	3C232	11	71	71	144	0.5	1465 $\pm$ 5	135 $\pm$ 9	-48 $\pm$ 9	80.8 $\pm$ 6.0	20.09 $\pm$ 0.02	[-134.4, -0.4]	[-136.5, -0.3]
11	NGC3067	SDSSJ095914.80+320357.0	128	40	71	144	0.5	1465 $\pm$ 5	135 $\pm$ 9	27 $\pm$ 5	28.4 $\pm$ 10.7	16.23 $\pm$ 1.43	[14.7, 124.7]	[10.2, 86.4]
12	NGC3198	RXJ1017.5+4702	370	58	73	217	1.7	660 $\pm$ 1	-145 $\pm$ 5	-37 $\pm$ 8	39.2 $\pm$ 15.0	13.18 $\pm$ 0.12	[-106.0, -30.9]	[-96.7, -19.0]
13	NGC3351	SDSSJ104335.90+115129.0	31	46	42	198	1.3	778 $\pm$ 4	-133 $\pm$ 11	-79 $\pm$ 19	78.6 $\pm$ 14.7	14.53 $\pm$ 0.12	[-93.5, -2.8]	[-128.3, -1.9]
14	NGC3432	CSO295	20	79	90	136	0.4	616 $\pm$ 4	119 $\pm$ 8	-16 $\pm$ 16	48.1 $\pm$ 12.0	15.05 $\pm$ 0.37	[0.3, 124.5]	[0.3, 141.3]
14	NGC3432	CSO295	20	79	90	136	0.4	616 $\pm$ 4	119 $\pm$ 8	46 $\pm$ 16	62.1 $\pm$ 9.9	15.18 $\pm$ 0.32	[0.3, 124.5]	[0.3, 141.3]
15	NGC3432	RXJ1054.2+3511	290	60	90	136	0.4	616 $\pm$ 4	119 $\pm$ 8	73 $\pm$ 14	66.8 $\pm$ 21.7	13.58 $\pm$ 0.12	[0.0, 0.1]	[30.4, 130.7]
16	NGC3631	RXJ1117.6+5301	78	78	17	139	0.5	1156 $\pm$ 1	42 $\pm$ 7	-26 $\pm$ 2	38.2 $\pm$ 2.6	14.21 $\pm$ 0.04	[0.4, 11.2]	[1.5, 40.2]
16	NGC3631	RXJ1117.6+5301	78	78	17	139	0.5	1156 $\pm$ 1	42 $\pm$ 7	109 $\pm$ 4	20.9 $\pm$ 9.5	13.17 $\pm$ 0.1	[0.4, 11.2]	[1.5, 40.2]
17	NGC3631	SBS1116+523	163	37	17	139	0.5	1156 $\pm$ 1	-42 $\pm$ 7	-125 $\pm$ 99	-99.0 $\pm$ -99.0	-99.0 $\pm$ -99.0	[-11.3, -2.3]	[-24.0, -7.9]
18	NGC3631	SDSSJ11443.70+525834.0	145	74	17	139	0.5	1156 $\pm$ 1	42 $\pm$ 7	2 $\pm$ 5	27.4 $\pm$ 8.7	13.52 $\pm$ 0.09	[0.7, 9.2]	[2.5, 29.5]
19	NGC3631	SDSSJ112448.30+531818.0	86	77	17	139	0.5	1156 $\pm$ 1	-42 $\pm$ 7	-138 $\pm$ 5	18.6 $\pm$ 9.4	13.18 $\pm$ 0.11	[-10.9, -0.4]	[-38.6, -1.8]
19	NGC3631	SDSSJ112448.30+531818.0	86	77	17	139	0.5	1156 $\pm$ 1	-42 $\pm$ 7	-21 $\pm$ 3	17.2 $\pm$ 4.0	13.7 $\pm$ 0.07	[-10.9, -0.4]	[-38.6, -1.8]
20	NGC3633	RXJ1121.2+0326	184	55	72	174	0.9	2587 $\pm$ 7	-149 $\pm$ 9	21 $\pm$ 16	36.3 $\pm$ 20.1	13.7 $\pm$ 0.18	[-128.2, -16.1]	[-107.4, -10.0]
21	NGC3666	SDSSJ12439.50+113117.0	58	86	78	154	0.6	1063 $\pm$ 2	-124 $\pm$ 6	-1 $\pm$ 3	36.0 $\pm$ 8.9	15.53 $\pm$ 0.67	[-120.0, -0.7]	[-129.3, -0.9]
22	NGC4529	MRK771	158	26	80	193	1.2	2536 $\pm$ 11	-104 $\pm$ 15	22 $\pm$ 11	33.0 $\pm$ 3.9	13.82 $\pm$ 0.04	[-111.2, -17.8]	[-124.9, -18.4]
23	NGC4565	RXJ1236.0+2641	147	38	86	229	2.0	1230 $\pm$ 5	252 $\pm$ 12	-23 $\pm$ 12	4.0 $\pm$ 12.4	13.03 $\pm$ 0.49	[-111.2, -17.8]	[-124.9, -18.4]
23	NGC4565	RXJ1236.0+2641	147	38	86	229	2.0	1230 $\pm$ 5	252 $\pm$ 12	-64 $\pm$ 6	26.8 $\pm$ 5.5	14.05 $\pm$ 0.12	[6.3, 14.7]	[14.9, 182.2]
24	NGC4939	PG1302-102	254	64	61	320	5.5	3093 $\pm$ 33	-205 $\pm$ 34	27 $\pm$ 7	16.6 $\pm$ 10.3	13.31 $\pm$ 0.14	[6.3, 14.7]	[14.9, 182.2]
25	NGC5786	QSO1500-4140	453	2	65	248	2.6	2975 $\pm$ 22	156 $\pm$ 23	356 $\pm$ 33	26.4 $\pm$ 3.6	13.23 $\pm$ 0.04	[-163.6, -23.3]	[-162.1, -9.0]
26	NGC5907	RBS1503	478	66	90	193	1.2	667 $\pm$ 3	-229 $\pm$ 6	-766 $\pm$ 99	-99.0 $\pm$ -99.0	-99.0 $\pm$ -99.0	[50.9, 161.2]	[33.8, 93.0]
27	NGC5951	2E1530+1511	55	88	74	203	1.4	1780 $\pm$ 1	127 $\pm$ 7	12 $\pm$ 3	48.5 $\pm$ 4.0	14.36 $\pm$ 0.05	[0.2, 121.4]	[0.2, 134.6]
27	NGC5951	2E1530+1511	55	88	74	203	1.4	1780 $\pm$ 1	127 $\pm$ 7	179 $\pm$ 4	39.8 $\pm$ 6.3	13.73 $\pm$ 0.05	[0.2, 121.4]	[0.2, 134.6]
28	NGC6140	MRK876	113	18	49	106	0.2	910 $\pm$ 4	104 $\pm$ 4	7 $\pm$ 6	49.2 $\pm$ 4.1	13.9 $\pm$ 0.06	[9.0, 78.2]	[24.1, 103.8]
28	NGC6140	MRK876	113	18	49	106	0.2	910 $\pm$ 4	104 $\pm$ 4	61 $\pm$ 5	27.4 $\pm$ 4.0	13.49 $\pm$ 0.15	[9.0, 78.2]	[24.1, 103.8]
29	NGC7817	MRK335	343	87	80	168	0.8	2309 $\pm$ 4	-178 $\pm$ 10	-360 $\pm$ 4	29.3 $\pm$ 0.9	13.8 $\pm$ 0.01	[-0.7, 0.8]	[-151.7, 204.4]
29	NGC7817	MRK335	343	87	80	168	0.8	2309 $\pm$ 4	-178 $\pm$ 10	-36 $\pm$ 4	43.3 $\pm$ 3.3	13.32 $\pm$ 0.03	[-0.7, 0.8]	[-151.7, 204.4]
30	UGC04238	PG0804+761	148	62	75	151	0.6	1544 $\pm$ 7	89 $\pm$ 12	-21 $\pm$ 7	36.7 $\pm$ 4.3	13.04 $\pm$ 0.04	[7.0, 85.5]	[12.7, 120.5]
30	UGC04238	PG0804+761	148	62	75	151	0.6	1544 $\pm$ 7	89 $\pm$ 12	67 $\pm$ 8	23.4 $\pm$ 7.1	12.6 $\pm$ 0.08	[7.0, 85.5]	[12.7, 120.5]
31	UGC06446	SDSSJ112448.30+531818.0	143	19	52	98	0.1	645 $\pm$ 1	62 $\pm$ 5	16 $\pm$ 3	39.8 $\pm$ 4.0	14.07 $\pm$ 0.04	[6.0, 50.0]	[18.7, 53.4]

Table 3 continued

Table 3 (*continued*)

#	Galaxy	Target	$\rho$ (kpc)	Az. (deg)	Inc. (deg)	$R_{vir}$ (kpc)	$L$ $L_*$	$v_{sys}$ (km s <sup>-1</sup> )	$v_{rot}^a$ (km s <sup>-1</sup> )	$\Delta v_{Ly\alpha}$ (km s <sup>-1</sup> )	$b$ (km s <sup>-1</sup> )	$\log N$	$v_{Steidel}^b$ (km s <sup>-1</sup> )	$v_{NFW}^c$ (km s <sup>-1</sup> )
(1)	(2)	(3)	(4)	(5)	(6)	(7)	(8)	(9)	(10)	(11)	(12)	(13)	(14)	(15)
32	UGC08146	PG1259+593	114	52	78	123	0.3	670 $\pm$ 1	80 $\pm$ 3	-49 $\pm$ 8	19.6 $\pm$ 8.4	13.04 $\pm$ 0.14	[2.9, 29.1]	[14.9, 101.7]
32	UGC08146	PG1259+593	114	52	78	123	0.3	670 $\pm$ 1	80 $\pm$ 3	23 $\pm$ 4	39.7 $\pm$ 4.8	13.72 $\pm$ 0.04	[2.9, 29.1]	[14.9, 101.7]
33	UGC09760	SDSSJ151237.15+012846.0	123	87	90	156	0.6	2094 $\pm$ 16	-54 $\pm$ 16	-69 $\pm$ 16	43.2 $\pm$ 7.1	14.5 $\pm$ 0.15	[-0.0, 0.0]	[-44.9, 42.3]

NOTE—

<sup>a</sup> Galaxy rotation velocity in the direction of the target in column 3.<sup>b</sup> Range of heliocentric velocities consistent with co-rotation from the Steidel et al. (2002) model<sup>c</sup> Range of heliocentric velocities consistent with co-rotation from the NFW halo model



#### 4. DISCUSSION

We present data on 33 galaxy-QSO systems, representing 47 individual Ly $\alpha$  component-galaxy pairs and 2 non-detections, for which we have galaxy information including kinematics, inclination, size and luminosity. This is the largest sample of its kind to date and provides the best yet opportunity to study the kinematic connection between galaxies and their neutral H I halos.

We designate each system as co-rotating or anti-rotating by comparing the absorption velocity difference,  $\Delta v = v_{\text{absorber}} - v_{\text{galaxy}}$ , to both the orientation of each galaxy and the model results. For example, the galaxy CGCG039-137 is probed on the receding side by sightline RX\_J1121.2+0326, with a  $\Delta v_{\text{Ly}\alpha} = 53 \text{ km s}^{-1}$  component detected. This  $\Delta v$  lies within the NFW model range ([1.6, 210.4]) as well as the Steidel ([1.1, 137.2]), and so is marked as "co-rotating" in all cases.

Table 3 summarizes our galaxy-absorber sample and includes the rotation velocity and associated error for each galaxy in Column (7), with the resulting co-rotation velocity ranges predicted from the Steidel et al. (2002) and NFW models given in Columns (10) and (11). In order to broadly account for velocity uncertainties we have calculated our model ranges to include the  $1\sigma$  rotation velocity errors. We note that the majority of our "co-rotating" sample fall well within the model ranges, so few would be thrown into uncertainty based on the relative size of included errors.

##### 4.1. Co-rotation Fraction

Here we consider in aggregate our sample of Ly $\alpha$  absorbers, and the fraction consistent with co-rotation under various constraints.

To start we consider the fraction of absorbers whose  $\Delta v$  velocity indicates they are on the "correct" side of the galaxy to be consistent with co-rotation. Based on their orientation and apparent velocities alone, we find 27/47 (57%) of absorbers have velocities consistent with co-rotation with the nearby galaxy. The Steidel et al. (2002) model produces 19/47 (40%), and the NFW model produces 23/47 (49%) consistent with co-rotation. Figure 4 presents maps of the locations of each absorber relative to its assumed host galaxy. In these figures we have rotated every system such that the galaxy major axes are horizontal with the approaching side on the left. Blue-diamonds indicate the absorber velocity as consistent with co-rotation, red-crosses indicate an anti-rotation, and open grey circles indicate non-detections. We have also scaled the size of each marker according to its relative column density, and annotated each with a number corresponding to the appropriate system number given in Column (1) of Table 3. Figure 4 also includes the same map zoomed in to a radius of  $1R_{\text{vir}}$ , as well as one each based on the Steidel et al. (2002) and cylindrical NFW model results.

A cursory look at the maps from Figure 4 reveals several interesting results. First, the highest column density

absorbers are all found within  $1R_{\text{vir}}$ . This is not surprising, given the results by numerous groups finding an impact parameter - column density anti-correlation (see e.g., French & Wakker 2017, and references therein). Second, just under half of our absorbers lie beyond  $1R_{\text{vir}}$ . Previously, most groups have concentrated on studying the sub- $1R_{\text{vir}}$  regime, but doing so may artificially truncate the full extent of the CGM. Third, just over half (12/23) of galaxies have either multiple distinct velocity components in a single QSO sightline, or multiple sightlines containing absorbers. Of these 12, 7 are oriented such that at least one component is co- and one anti-rotating with the galaxy.

However, a more in-depth look at the data reveals a number of these absorbers have  $\Delta v$  much larger than the inclination-corrected galaxy rotation velocity ( $v_{\text{rot}}$ ). In other words, the velocity of the absorber relative to galaxy systemic is much greater than the rotation velocity of the galaxy disk. This results in a much smaller fraction of co-rotating absorbers when compared to our models, which will never output a velocity *higher* than  $v_{\text{rot}}$ . In undertaking this study we necessarily must begin by assuming that absorption within some velocity limit and impact parameter from a galaxy is likely associated with that galaxy. To start with we set these limits at  $\Delta v_{\text{max}} = 400 \text{ km s}^{-1}$  and  $\rho_{\text{max}} = 3R_{\text{vir}}$ , but now let us consider a stricter velocity range.

We next consider only absorbers with  $|\Delta v| \leq v_{\text{rot}}$ , or absorbers with velocities differences no greater than the maximal galaxy rotation velocity (in other words we are only considering absorbers where  $|v_{\text{Ly}\alpha} - v_{\text{sys}}| \leq v_{\text{rot}}$ , which are those absorbers within the velocity range of  $\pm$  rotation – this constraint removes 8 from our original sample of 47 absorbers). This constraint just means we only consider those absorbers for which it is *a-priori* possible to be found as co-rotating. In the full sample, lines not meeting this criterion would *always* be classified as non-rotating. Hence, we are effectively just setting the  $\Delta v$  velocity separation limit on a case-by case basis informed by each galaxy instead of globally given the additional information available. We could just as easily have started this study by looking for only absorbers within  $\Delta v = 150 \text{ km s}^{-1}$  of a galaxy instead of  $\Delta v = 400 \text{ km s}^{-1}$ , which would have a similar overall effect. This criteria instead narrows the focus to only those absorbers kinematically close enough to a galaxy to test for a co-rotation fraction with minimal contamination from Ly $\alpha$  forest lines.

With this rotation-based velocity constraint in place the co-rotating fractions for the Steidel et al. (2002) and our NFW models increase to 19/39 (49%) and 23/39 (59%), while the apparent co-rotation fraction also increases slightly to 24/39 (62%). Consistently, we find our NFW model to predict an  $\sim 8 - 10\%$  higher co-rotation fraction than the Steidel et al. (2002) model, and similar to the apparent velocity results. This is a not wholly unexpected, and yet refreshing result; simulations have

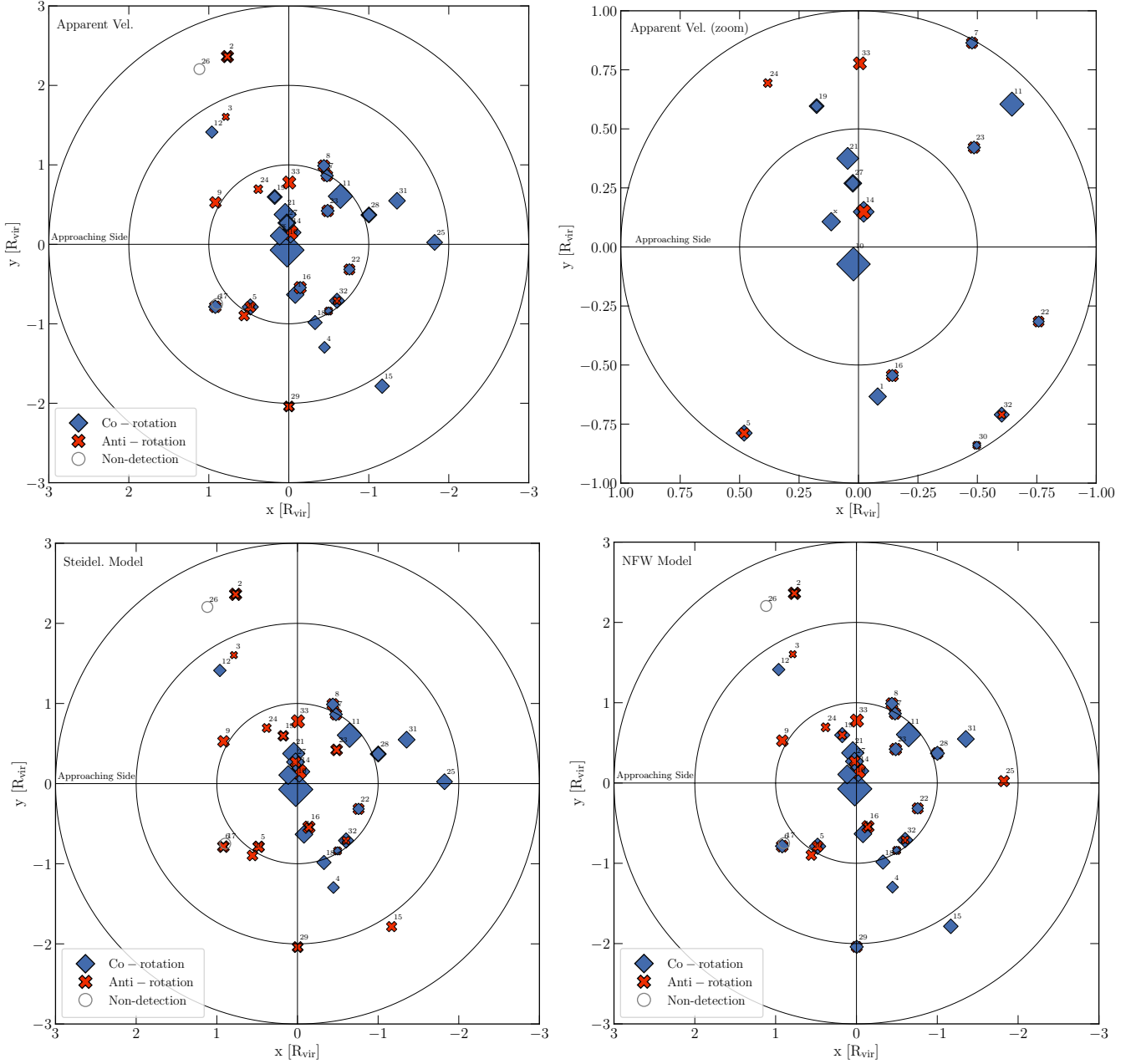


**Figure 2. All:** Maps of the locations of each absorber normalized with respect to the galaxy virial radius. The color and style of each point indicates the line-of-sight velocity compared to that of the rotation of the nearby galaxy. Blue diamonds indicate absorbers whose  $\Delta v$  sign aligns with the galaxy rotation (i.e., consistent with co-rotation), red crosses indicate anti-alignment, and grey open circles indicate non-detections. The size of each point is scaled to reflect the column density of the absorber. All galaxies are rotated to  $\text{PA} = 90^\circ$  or  $270^\circ$ , such that their major axis' are horizontal and their approaching side is on the left as indicated. The number identifiers correspond to the system number given in column (1) of Table 3. Concentric rings indicate distances of 1, 2, and 3  $R_{\text{vir}}$ . **Top-Left:** Results based on apparent velocity on-sky only (model independent). **Top-Right:** A zoom in showing only those systems within  $1R_{\text{vir}}$ . Concentric rings indicate distances of 0.5 and  $1R_{\text{vir}}$ . **Bottom-Left:** Results based on the model from Steidel et al. (2002). **Bottom-Right:** Results based on our cylindrical NFW model.

predicted that galaxies are strongly linked to their surroundings and share angular momentum, which should result in a higher than 50% halo-gas co-rotation fraction.

#### 4.2. Co-rotation as a function of $L^*$

For brevity's sake we will concentrate only on the NFW model results with our  $|\Delta v| \leq v_{\text{rot}}$  restriction

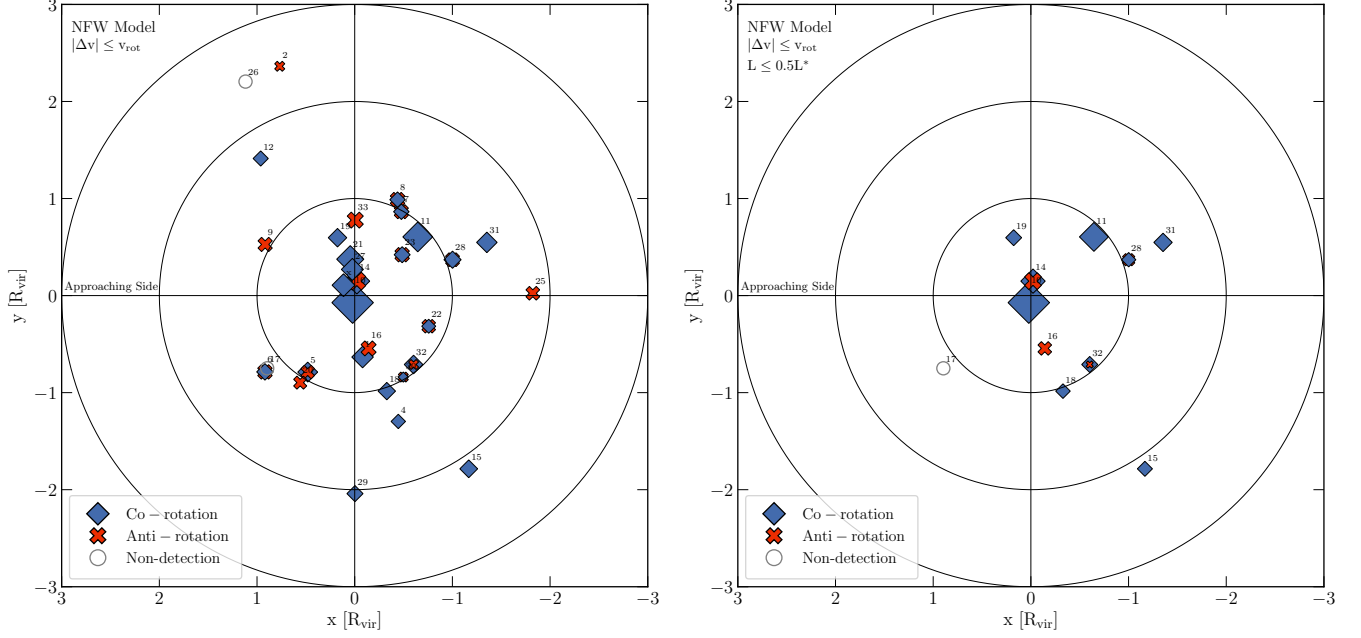


**Figure 3. Left:** A map of the locations of each absorber normalized with respect to the galaxy virial radius. The color and style of each point indicates the NFW rotation model results for each absorber with a  $|\Delta v| \leq v_{\text{rot}}$  constraint imposed. Concentric rings indicate distances of 1, 2, and 3  $R_{\text{vir}}$ . Blue diamonds indicate co-rotation, red crosses indicate anti-rotation, and grey circles indicate cases where either is possible due to a combination of orientation and velocity uncertainties. The size of each point is scaled to reflect the EW of the absorber. All galaxies are rotated to  $\text{PA} = 90^\circ$  or  $270^\circ$ , such that their major axis' are horizontal and their approaching side is on the left as indicated. The number identifiers correspond to the system number given in column (1) of Table 3. **Right:** The same map as **left**, but includes only those absorbers near  $L^* \leq 0.6$  galaxies.

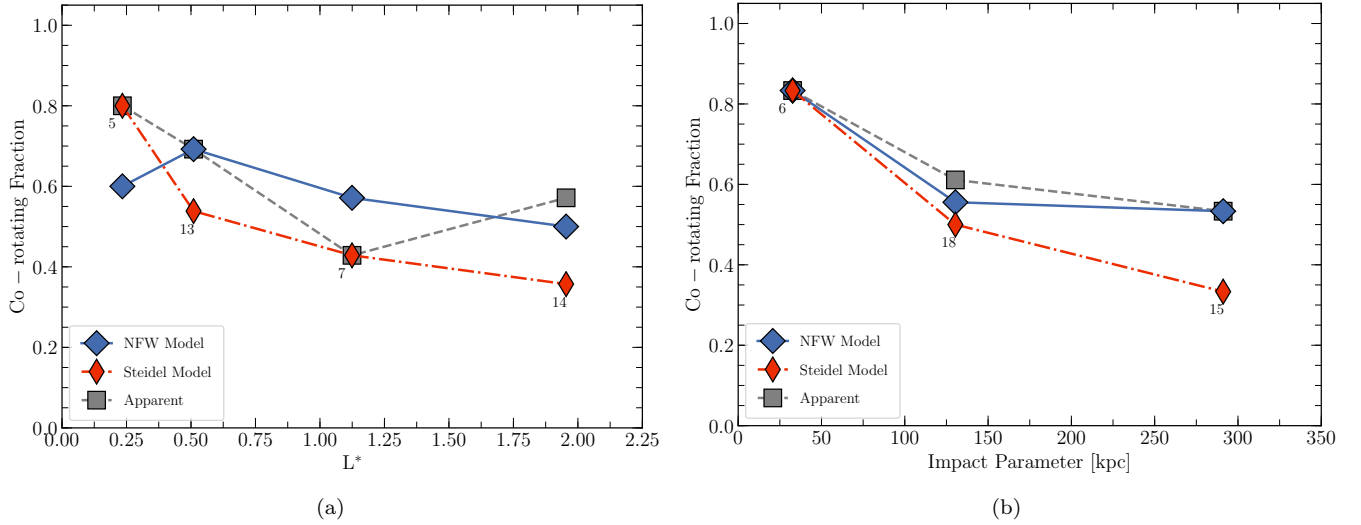


**Figure 4. Left:** The fraction of co-rotating absorbers as a function of  $L^*$ . **Right:** The fraction of co-rotating absorbers as a function of impact parameter. **All:** Grey squares corresponding to model-independent apparent velocity results, thin-red diamonds correspond to [Steidel et al. \(2002\)](#) model results, and thick-blue diamonds correspond to our NFW model results. Bin edges are calculated to yield approximately equally sized bins. The numbers underneath each red-diamond show the number of absorber-galaxy systems in each bin.

from here on-wards. We consider the effect of galaxy

luminosity on co-rotation fraction by first separating our

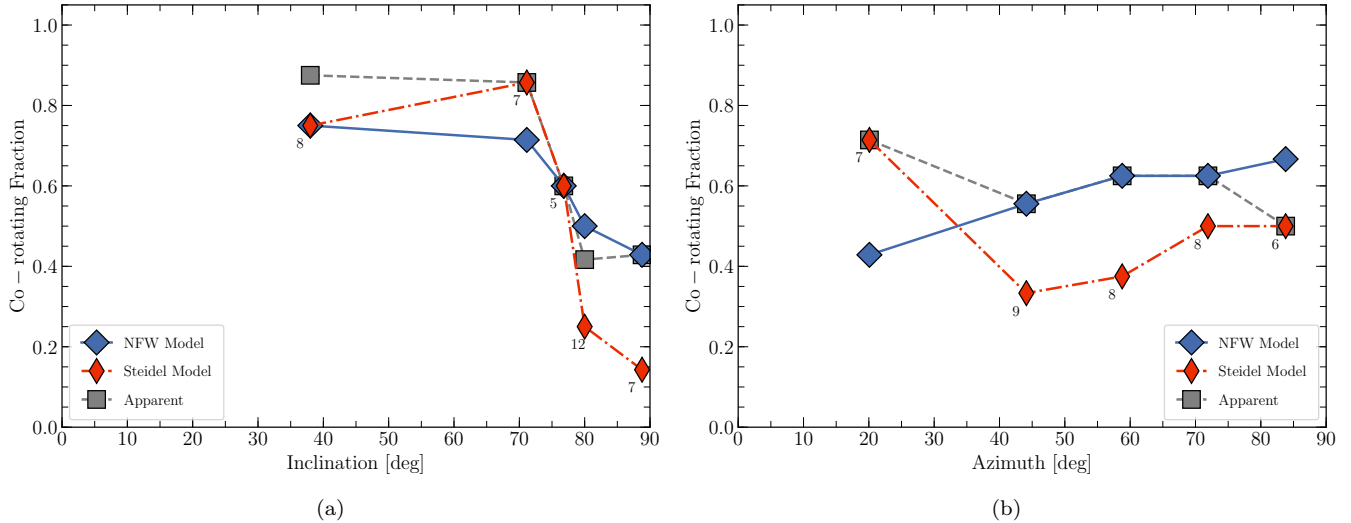


**Figure 5.** The co-rotation fraction as a function of inclination angle (**left**) and azimuth angle (**right**) for  $|\Delta v| \leq v_{\text{rot}}$  absorbers. Results from apparent on-sky velocity are shown as grey-squares, Steidel model results as thin red-diamonds, and our NFW model results as thick blue-diamonds. Bins are chosen algorithmically to produce approximately even bins. Thus the first inclination bin appears at  $\sim 40$  degrees because we have mostly highly inclined galaxies.

sample around  $0.5L^*$ . This results in 13 absorbers near  $L \leq 0.5L^*$  galaxies and 26 around more luminous galaxies. The co-rotating fraction around luminous galaxies is then 54%, compared to 69% around  $L \leq 0.5L^*$  galaxies. Figure 4.1 shows absorbers map for this  $L \leq 0.5L^*$  galaxies subsample (right) compared to the full sample (left).

Furthermore, we find this co-rotation fraction smoothly decreases as a function of  $L^*$ , as shown in Figure 5(a). In this figure we have binned galaxy-absorber systems into 4 bins of luminosity, and are plotting the corresponding co-rotation fraction for each bin. This uneven bin spacing was chosen algorithmically to produce relatively evenly sized bins, and the exact binning does not affect the overall trend. Unfortunately there are a large number of systems between  $1.7 - 1.8 L^*$ , so no splitting exists to produce perfectly even bins. The bin sizes are labeled explicitly underneath each data point for clarity.

Given recent simulation results suggesting that co-rotating accretion gas is predominately cold-mode for low-mass galaxies in the local Universe, this may be a signature of this co-rotating, cold-mode accreting gas. Additionally, Lutz et al. (2018) find that galaxies with high H I mass compared to their stellar mass have higher halo angular momentum, which may be impeding their ability to efficiently form stars. While we do not have independent measures of H I and stellar mass for our galaxies, it may not be unreasonable to think that such lower stellar-mass galaxies are analogous to the low luminosity galaxies in our sample.

Finally, we show in Figure 5(b) co-rotation fraction as a function of impact parameter. For all three cases we consistently find declining co-rotation fraction at greater physical distances from galaxies. Within  $\sim 100$  kpc, over

80% of Ly $\alpha$  absorbers have velocities consistent with co-rotation, compared to  $\sim 50\%$  beyond this distance.

#### 4.3. Inclination & Azimuth

Here we investigate how the inclination of each galaxy affects the co-rotation rate. Figures 4 and 5(b) show the co-rotation fraction for each model as a function of inclination and azimuth angle. The co-rotation fraction is largely invariant as a function of azimuth angle but sharply drops off above inclinations of  $\sim 70$  degrees, while remaining mostly flat below that. The Steidel et al. (2002) model in particular predicts  $\lesssim 20\%$  co-rotation rate for highly inclined galaxies, which is less than half that predicted by our NFW model or apparent velocity ( $\sim 40\%$ ). Hence, this simple monolithic disk model is likely not physical.

Numerous simulations (e.g., Stewart et al. 2011b and Ho et al. 2019) and metal line absorption studies (e.g., Kacprzak et al. 2010, Martin et al. 2019) suggest that co-rotation should instead *peak* around the major axis of highly inclined galaxies. Our results may differ for several reasons. First, we simply do not have many systems that are both highly inclined and aligned along the major axis. Of the 30 components associated with galaxies inclined  $70^\circ$  or more, only 8 are within  $45^\circ$  of the major axis. We do not otherwise see a strong correlation with azimuth angle, but there may be a combination of azimuth and inclination effects present which are difficult to untangle. Second, our sample consists almost entirely of low column density gas, whereas the Mg II absorbers in other studies trace much denser material. As simulations suggest that cold, dense gas accretes mostly along an extended,

warped disk, the more diffuse gas we are tracing may be more geometrically and kinematically complex.

#### 4.4. Doppler $b$ -parameters

Here we consider the Doppler  $b$ -parameters of our absorber sample. In Figure 6 we show how the  $b$ -parameters vary as a function of  $\Delta v$  for co-rotating versus anti-rotating absorbers (based on our NFW model results and limited to  $|\Delta v| \leq v_{\text{rot}}$  absorber). Figure 6 also includes marginal histograms to show the distribution of  $b$  and  $\Delta v$ . We might expect the co-rotating sample to occupy a narrower  $\Delta v$  space based on their definition ( $\Delta v$  fitting within the velocity bounds given by our NFW model), but the elevated  $b$ -parameters for these compared to the relatively flat distribution for anti-rotators is intriguing. All the anti-rotators have  $b \lesssim 50 \text{ km s}^{-1}$ , leaving all 5 broader lines as co-rotating systems.

As previously discussed however, the picture described by the simulations of [Stewart et al. \(2011b\)](#) and others describes a scenario where co-rotating gas is predominately the product of cold-mode accretion. Hotter, and thus broader, outflowing gas would likely carry angular momentum from the disk with it, but this would be quickly lost as the outflows expand into the halo and result in negligible observable rotation signature. Indeed, as shown in Figure 7, there is a slight correlation between  $b$  and azimuth angle, with the broadest absorbers within  $\sim 50^\circ$  of the minor axis.

As the broadest lines are higher than expected for purely thermal motions within a single Ly $\alpha$  structure, we may be observing either a number of clouds that are close in velocity space or a filament with a range of turbulent, internal velocities. In this scenario these high  $b$ -parameters could be consistent with filamentary inflows versus around higher  $L^*$  galaxies where virial shocks are perhaps breaking larger structures into smaller, more isolated cloudlets and producing lower  $b$ -parameter absorption.

To further explore this, we now consider the 9 galaxies for which we find multiple Ly $\alpha$  components. Figure 8 shows the  $b$  and  $\log N(\text{H I})$  distributions for each of these galaxies. Intriguingly, for 8/9 of these galaxies have at one component consistent with both co-rotation and anti-rotation. Of these 8, 6 are orientated such the lower  $b$  component is co-rotating, and 7/8 such that the lower  $\log N(\text{H I})$  component is co-rotating. Hence, narrower, lower column density components appear more likely to be co-rotating. Once again these results differ from numerous metal line kinematic studies finding the entirety of Mg II absorption tends to lie on one side of galaxies systemic velocities (e.g., [Kacprzak et al. 2010](#), [Ho et al. 2017](#)). Galaxies halo are thus likely multiphase, with distributions of material complex both geometrically and kinematically.

## 5. SUMMARY

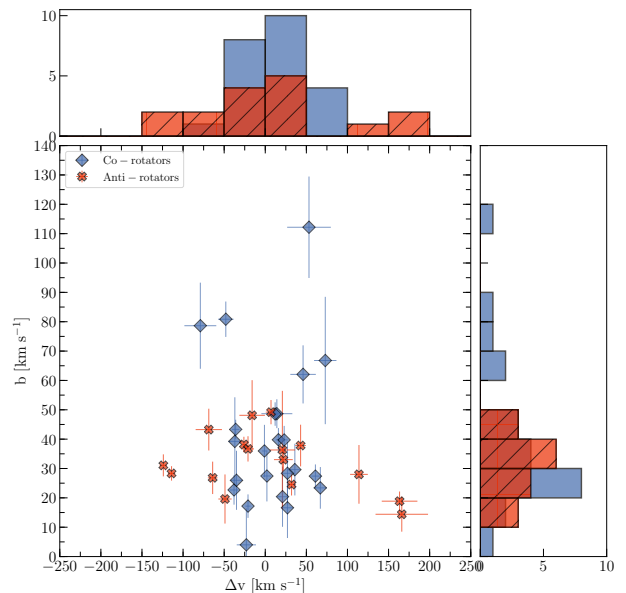


**Figure 6.** The Doppler  $b$  parameters for  $|\Delta v| \leq v_{\text{rot}}$  absorbers as a function of  $\Delta v$ . The co-rotating (blue diamonds) and anti-rotating (red crosses) designation is based on our NFW model results. The marginal histograms show the distributions of  $b$  and  $\Delta v$  similarly split into co-rotating (blue) and anti-rotating (red).

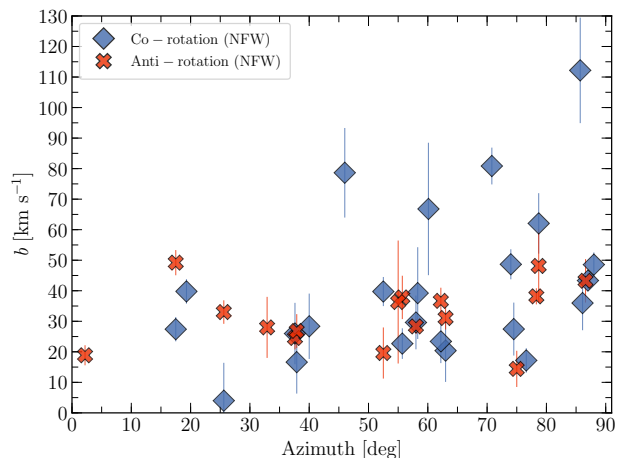


**Figure 7.** The Doppler  $b$  parameters for  $|\Delta v| \leq v_{\text{rot}}$  absorbers as a function of azimuth angle. The co-rotating (blue diamonds) and anti-rotating (red crosses) designation is based on our NFW model results.

We have presented complimentary COS Ly $\alpha$  absorption-line and nearby galaxy rotation curve analysis for a sample of 33 galaxy-QSO pairs, including 47 Ly $\alpha$  components, resulting in the largest yet sample of its kind. Overall, our findings suggest that halo rotation is only one of many factors contributing to the velocity distribution of Ly $\alpha$  clouds near galaxies. The fact that we see coherent co-rotation trends with galaxy luminosity,



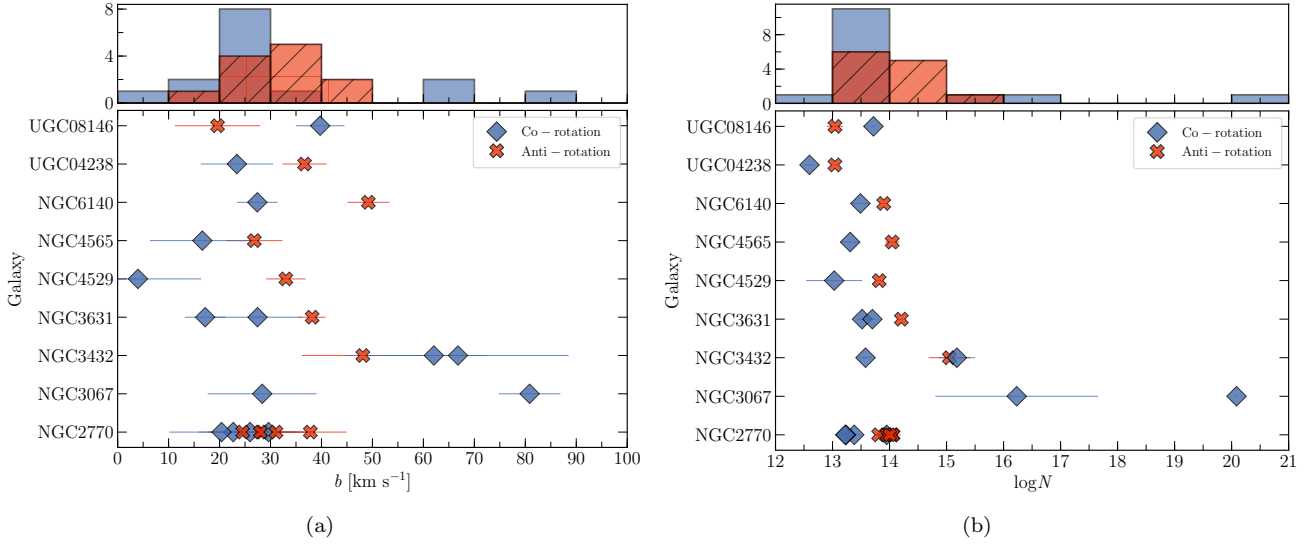


**Figure 8.** The Doppler  $b$  parameters and column densities for  $|\Delta v| \leq v_{\text{rot}}$  absorbers where *multiple components are associated with a single galaxy*. The co-rotating (blue diamonds) and anti-rotating (red crosses) designation is based on our NFW model results. The top histogram shows the distribution of  $b$  similarly split into co-rotating (blue) and anti-rotating (red).

impact parameter, and orientation suggests that these absorbers do know about the halo rotation. The effect of outflow, inflow, and turbulent velocities certainly also plays an important role, and one that is extremely difficult to untangle. Our main conclusions are the summarized below:

1. The fraction of Ly $\alpha$  absorbers appearing to co-rotate with the nearby galaxy declines as a function galaxy luminosity ( $L^*$ ) and distance ( $\rho$ ). Our overall co-rotation fraction is broadly consistent with the simulation results of [Stewart et al. \(2011b, 2013\)](#), and effect of galaxy luminosity on halo gas co-rotation is consistent with predicted cold-mode filamentary accretion schemes.

2. The co-rotation fraction is mostly inclination-independent until  $i \sim 70$  degrees, at which point it sharply declines. WHAT DOES THIS MEAN?

3. Based on the predicted velocity of our NFW halo model, 69% of absorbers co-rotate around  $\leq 0.5L^*$  galaxies, which falls down to 54% around more luminous galaxies at  $z \sim 0$ .

4. Co-rotating absorbers (when chosen from the sample restricted to  $|\Delta v| \leq v_{\text{rot}}$ ) occupy a wide range in Doppler  $b$ -parameter, while anti-rotators have mostly  $b \leq 50 \text{ km s}^{-1}$ . However, for galaxies with multiple sightlines, 8/9 have both a co-rotating and anti-rotating absorber. Among this subsample, the co-rotating absorbers have both lower  $b$  values and lower column densities in 6/8 and 7/8 cases (respectively).

D. M. F. thanks Claire Murray for useful insights, particularly related to our halo model, and Julie Davis for invaluable SALT data reduction pointers. This research has made use of the NASA/IPAC Extragalactic Database (NED) which is operated by the Jet Propulsion Laboratory, California Institute of Technology, under contract with the National Aeronautics and Space Administration. Based on observations with the NASA/ESA *Hubble Space Telescope*, obtained at the Space Telescope Science Institute (STScI), which is operated by the Association of Universities for Research in Astronomy, Inc., under NASA contract NAS 5-26555. Spectra were retrieved from the Barbara A. Mikulski Archive for Space Telescopes (MAST) at STScI. Some of the observations reported in this paper were obtained with the Southern African Large Telescope (SALT) under program 2016-1-SCI-062 (PI: Wakker). Over the course of this study, D.M.F. and B.P.W. were supported by grant AST-1108913 from the National Science Foundation and GO-13444.01-A, GO-14240.01-A, and AR-14577.01-A from the Space Telescope Science Institute.

*Facility:* HST (COS), SALT (RSS)



**Table 4.** CGM Rotation: Summary of Results

Sub-sample	Co-rotating	Anti-rotating	Co-rotating	Anti-rotating	Co-rotating	Anti-rotating
			$\rho \leq 1$	$\rho \leq 1$	$\rho > 1$	$\rho > 1$
Apparent Vel.	27	20	17	10	10	10
Steidel Model	19	28	11	16	8	12
NFW Model	23	24	10	12	15	19
With Constraint: $ \Delta v  \leq v_{\text{rot}}$						
Apparent Vel.	24	15	14	9	10	6
Steidel Model	19	20	11	12	8	8
NFW Model	23	16	14	9	9	7
With Constraint: $ \Delta v  \leq v_{\text{rot}}$ $[0 \leq L^* \leq 0.5]$						
Apparent Vel.	9	4	5	3	4	1
Steidel Model	8	5	4	4	4	1
NFW Model	23	16	14	9	9	7
With Constraint: $ \Delta v  \leq v_{\text{rot}}$ $[L^* > 0.5]$						
Apparent Vel.	14	12	9	6	5	6
Steidel Model	11	15	7	8	4	7
NFW Model	14	12	9	6	5	6

## REFERENCES

- Abazajian, K., Adelman-McCarthy, J. K., Agüeros, M. A., et al. 2005, *AJ*, 129, 1755, doi: [10.1086/427544](https://doi.org/10.1086/427544)
- Bertschinger, E. 1985, *ApJS*, 58, 39, doi: [10.1086/191028](https://doi.org/10.1086/191028)
- Birnboim, Y., & Dekel, A. 2003, *MNRAS*, 345, 349, doi: [10.1046/j.1365-8711.2003.06955.x](https://doi.org/10.1046/j.1365-8711.2003.06955.x)
- Bouché, N., Murphy, M. T., Kacprzak, G. G., et al. 2013, *Science*, 341, 50, doi: [10.1126/science.1234209](https://doi.org/10.1126/science.1234209)
- Bouché, N., Finley, H., Schroetter, I., et al. 2016, *ApJ*, 820, 121, doi: [10.3847/0004-637X/820/2/121](https://doi.org/10.3847/0004-637X/820/2/121)
- Bowen, D. V., Chelouche, D., Jenkins, E. B., et al. 2016, *ApJ*, 826, 50, doi: [10.3847/0004-637X/826/1/50](https://doi.org/10.3847/0004-637X/826/1/50)
- Brook, C. B., Governato, F., Roškar, R., et al. 2011, *MNRAS*, 415, 1051, doi: [10.1111/j.1365-2966.2011.18545.x](https://doi.org/10.1111/j.1365-2966.2011.18545.x)
- Brooks, A. M., Governato, F., Quinn, T., Brook, C. B., & Wadsley, J. 2009, *ApJ*, 694, 396, doi: [10.1088/0004-637X/694/1/396](https://doi.org/10.1088/0004-637X/694/1/396)
- Buckley, D. A. H., Swart, G. P., & Meiring, J. G. 2006, in *Proc. SPIE, Vol. 6267, Society of Photo-Optical Instrumentation Engineers (SPIE) Conference Series*, 62670Z
- Burgh, E. B., Nordsieck, K. H., Kobulnicky, H. A., et al. 2003, in *Proc. SPIE, Vol. 4841, Instrument Design and Performance for Optical/Infrared Ground-based Telescopes*, ed. M. Iye & A. F. M. Moorwood, 1463–1471
- Carilli, C. L., van Gorkom, J. H., & Stocke, J. T. 1989, *Nature*, 338, 134, doi: [10.1038/338134a0](https://doi.org/10.1038/338134a0)
- Charlton, J. C., & Churchill, C. W. 1998, *ApJ*, 499, 181, doi: [10.1086/305632](https://doi.org/10.1086/305632)
- Chen, D. N., Jing, Y. P., & Yoshikawa, K. 2003, *ApJ*, 597, 35, doi: [10.1086/378379](https://doi.org/10.1086/378379)
- Corwin, Jr., H. G., Buta, R. J., & de Vaucouleurs, G. 1994, *AJ*, 108, 2128, doi: [10.1086/117225](https://doi.org/10.1086/117225)
- Côté, S., Wyse, R. F. G., Carignan, C., Freeman, K. C., & Broadhurst, T. 2005, *ApJ*, 618, 178, doi: [10.1086/425853](https://doi.org/10.1086/425853)
- Crawford, S. M., Still, M., Schellart, P., et al. 2010, in *Proc. SPIE, Vol. 7737, Observatory Operations: Strategies, Processes, and Systems III*, 773725
- Danovich, M., Dekel, A., Hahn, O., & Teyssier, R. 2012, *MNRAS*, 422, 1732, doi: [10.1111/j.1365-2966.2012.20751.x](https://doi.org/10.1111/j.1365-2966.2012.20751.x)
- de Blok, W. J. G., Walter, F., Brinks, E., et al. 2008, *AJ*, 136, 2648, doi: [10.1088/0004-6256/136/6/2648](https://doi.org/10.1088/0004-6256/136/6/2648)
- Dekel, A., & Birnboim, Y. 2006, *MNRAS*, 368, 2, doi: [10.1111/j.1365-2966.2006.10145.x](https://doi.org/10.1111/j.1365-2966.2006.10145.x)
- Dekel, A., Birnboim, Y., Engel, G., et al. 2009, *Nature*, 457, 451, doi: [10.1038/nature07648](https://doi.org/10.1038/nature07648)
- di Nella, H., Paturel, G., Walsh, A. J., et al. 1996, *A&AS*, 118, 311
- Diamond-Stanic, A. M., Coil, A. L., Moustakas, J., et al. 2016, *ApJ*, 824, 24, doi: [10.3847/0004-637X/824/1/24](https://doi.org/10.3847/0004-637X/824/1/24)
- Dicaire, I., Carignan, C., Amram, P., et al. 2008, *MNRAS*, 385, 553, doi: [10.1111/j.1365-2966.2008.12868.x](https://doi.org/10.1111/j.1365-2966.2008.12868.x)
- El-Badry, K., Quataert, E., Wetzel, A., et al. 2018, *MNRAS*, 473, 1930, doi: [10.1093/mnras/stx2482](https://doi.org/10.1093/mnras/stx2482)
- Falco, E. E., Kurtz, M. J., Geller, M. J., et al. 1999, *PASP*, 111, 438, doi: [10.1086/316343](https://doi.org/10.1086/316343)
- Fillmore, J. A., & Goldreich, P. 1984, *ApJ*, 281, 1, doi: [10.1086/162070](https://doi.org/10.1086/162070)
- French, D. M., & Wakker, B. P. 2017, *ApJ*, 837, 138, doi: [10.3847/1538-4357/aa6111](https://doi.org/10.3847/1538-4357/aa6111)
- Giovanelli, R., Avera, E., & Karachentsev, I. D. 1997, *AJ*, 114, 122, doi: [10.1086/118459](https://doi.org/10.1086/118459)
- Green, J. C., Froning, C. S., Osterman, S., et al. 2012, *ApJ*, 744, 60, doi: [10.1088/0004-637X/744/1/60](https://doi.org/10.1088/0004-637X/744/1/60)
- Grogan, N. A., Geller, M. J., & Huchra, J. P. 1998, *ApJS*, 119, 277, doi: [10.1086/313164](https://doi.org/10.1086/313164)
- Ho, S. H., Martin, C. L., Kacprzak, G. G., & Churchill, C. W. 2017, *ApJ*, 835, 267, doi: [10.3847/1538-4357/835/2/267](https://doi.org/10.3847/1538-4357/835/2/267)
- Ho, S. H., Martin, C. L., & Turner, M. L. 2019, *ApJ*, 875, 54, doi: [10.3847/1538-4357/ab0ec2](https://doi.org/10.3847/1538-4357/ab0ec2)
- Huchra, J. P., & Geller, M. J. 1982, *ApJ*, 257, 423, doi: [10.1086/160000](https://doi.org/10.1086/160000)
- Jones, D. H., Read, M. A., Saunders, W., et al. 2009, *MNRAS*, 399, 683, doi: [10.1111/j.1365-2966.2009.15338.x](https://doi.org/10.1111/j.1365-2966.2009.15338.x)
- Kacprzak, G. G. 2017, *Astrophysics and Space Science Library*, Vol. 430, *Gas Accretion in Star-Forming Galaxies*, ed. A. Fox & R. Davé, 145
- Kacprzak, G. G., Churchill, C. W., Barton, E. J., & Cooke, J. 2011, *ApJ*, 733, 105, doi: [10.1088/0004-637X/733/2/105](https://doi.org/10.1088/0004-637X/733/2/105)
- Kacprzak, G. G., Churchill, C. W., Ceverino, D., et al. 2010, *ApJ*, 711, 533, doi: [10.1088/0004-637X/711/2/533](https://doi.org/10.1088/0004-637X/711/2/533)
- Keeney, B. A., Momjian, E., Stocke, J. T., Carilli, C. L., & Tumlinson, J. 2005, *ApJ*, 622, 267, doi: [10.1086/427899](https://doi.org/10.1086/427899)
- Kereš, D., Katz, N., Weinberg, D. H., & Davé, R. 2005, *MNRAS*, 363, 2, doi: [10.1111/j.1365-2966.2005.09451.x](https://doi.org/10.1111/j.1365-2966.2005.09451.x)
- Kimm, T., Slyz, A., Devriendt, J., & Pichon, C. 2011, *MNRAS*, 413, L51, doi: [10.1111/j.1745-3933.2011.01031.x](https://doi.org/10.1111/j.1745-3933.2011.01031.x)
- Knapen, J. H. 1997, *MNRAS*, 286, 403, doi: [10.1093/mnras/286.2.403](https://doi.org/10.1093/mnras/286.2.403)
- Kobulnicky, H. A., Nordsieck, K. H., Burgh, E. B., et al. 2003, in *Proc. SPIE, Vol. 4841, Instrument Design and Performance for Optical/Infrared Ground-based Telescopes*, ed. M. Iye & A. F. M. Moorwood, 1634–1644
- Koribalski, B. S., Staveley-Smith, L., Kilborn, V. A., et al. 2004, *AJ*, 128, 16, doi: [10.1086/421744](https://doi.org/10.1086/421744)
- Krogager, J.-K. 2018, *ArXiv e-prints*. <https://arxiv.org/abs/1803.01187>

- Lu, N. Y., Hoffman, G. L., Groff, T., Roos, T., & Lamphier, C. 1993, *ApJS*, 88, 383, doi: [10.1086/191826](https://doi.org/10.1086/191826)
- Lutz, K. A., Kilborn, V. A., Koribalski, B. S., et al. 2018, *MNRAS*, 476, 3744, doi: [10.1093/mnras/sty387](https://doi.org/10.1093/mnras/sty387)
- Martin, C. L., Ho, S. H., Kacprzak, G. G., & Churchill, C. W. 2019, *ApJ*, 878, 84, doi: [10.3847/1538-4357/ab18ac](https://doi.org/10.3847/1538-4357/ab18ac)
- Marzke, R. O., Huchra, J. P., & Geller, M. J. 1994, *ApJ*, 428, 43, doi: [10.1086/174218](https://doi.org/10.1086/174218)
- Mathewson, D. S., & Ford, V. L. 1996, *ApJS*, 107, 97, doi: [10.1086/192356](https://doi.org/10.1086/192356)
- Narayanan, A., Wakker, B. P., Savage, B. D., et al. 2010, *ApJ*, 721, 960, doi: [10.1088/0004-637X/721/2/960](https://doi.org/10.1088/0004-637X/721/2/960)
- Navarro, J. F., Frenk, C. S., & White, S. D. M. 1996, *ApJ*, 462, 563, doi: [10.1086/177173](https://doi.org/10.1086/177173)
- . 1997, *ApJ*, 490, 493, doi: [10.1086/304888](https://doi.org/10.1086/304888)
- Ocvirk, P., Pichon, C., & Teyssier, R. 2008, *MNRAS*, 390, 1326, doi: [10.1111/j.1365-2966.2008.13763.x](https://doi.org/10.1111/j.1365-2966.2008.13763.x)
- O'Donoghue, D., Buckley, D. A. H., Balona, L. A., et al. 2006, *MNRAS*, 372, 151, doi: [10.1111/j.1365-2966.2006.10834.x](https://doi.org/10.1111/j.1365-2966.2006.10834.x)
- Pichon, C., Pogosyan, D., Kimm, T., et al. 2011, *MNRAS*, 418, 2493, doi: [10.1111/j.1365-2966.2011.19640.x](https://doi.org/10.1111/j.1365-2966.2011.19640.x)
- Powell, L. C., Slyz, A., & Devriendt, J. 2011, *MNRAS*, 414, 3671, doi: [10.1111/j.1365-2966.2011.18668.x](https://doi.org/10.1111/j.1365-2966.2011.18668.x)
- Rhee, M.-H., & van Albada, T. S. 1996, *A&AS*, 115, 407
- Rubin, V. C., Thonnard, N. T., & Ford, Jr., W. K. 1982, *AJ*, 87, 477, doi: [10.1086/113120](https://doi.org/10.1086/113120)
- Sharma, S., & Steinmetz, M. 2005, *ApJ*, 628, 21, doi: [10.1086/430660](https://doi.org/10.1086/430660)
- Shen, S., Madau, P., Guedes, J., et al. 2013, *ApJ*, 765, 89, doi: [10.1088/0004-637X/765/2/89](https://doi.org/10.1088/0004-637X/765/2/89)
- Sofue, Y. 1996, *ApJ*, 458, 120, doi: [10.1086/176796](https://doi.org/10.1086/176796)
- Steidel, C. C., Kollmeier, J. A., Shapley, A. E., et al. 2002, *ApJ*, 570, 526, doi: [10.1086/339792](https://doi.org/10.1086/339792)
- Stevens, A. R. H., Lagos, C. d. P., Contreras, S., et al. 2017, *MNRAS*, 467, 2066, doi: [10.1093/mnras/stx243](https://doi.org/10.1093/mnras/stx243)
- Stewart, K. R., Brooks, A. M., Bullock, J. S., et al. 2013, *ApJ*, 769, 74, doi: [10.1088/0004-637X/769/1/74](https://doi.org/10.1088/0004-637X/769/1/74)
- Stewart, K. R., Kaufmann, T., Bullock, J. S., et al. 2011a, *ApJL*, 735, L1, doi: [10.1088/2041-8205/735/1/L1](https://doi.org/10.1088/2041-8205/735/1/L1)
- . 2011b, *ApJ*, 738, 39, doi: [10.1088/0004-637X/738/1/39](https://doi.org/10.1088/0004-637X/738/1/39)
- Stewart, K. R., Maller, A. H., Oñorbe, J., et al. 2017, *ApJ*, 843, 47, doi: [10.3847/1538-4357/aa6dff](https://doi.org/10.3847/1538-4357/aa6dff)
- Stocke, J. T., Keeney, B. A., & Danforth, C. W. 2010, *PASA*, 27, 256, doi: [10.1071/AS09074](https://doi.org/10.1071/AS09074)
- Stocke, J. T., Keeney, B. A., Danforth, C. W., et al. 2013, *ApJ*, 763, 148, doi: [10.1088/0004-637X/763/2/148](https://doi.org/10.1088/0004-637X/763/2/148)
- Swaters, R. A., Sancisi, R., van Albada, T. S., & van der Hulst, J. M. 2009, *A&A*, 493, 871, doi: [10.1051/0004-6361:200810516](https://doi.org/10.1051/0004-6361:200810516)
- van de Voort, F., Schaye, J., Booth, C. M., Haas, M. R., & Dalla Vecchia, C. 2011, *MNRAS*, 414, 2458, doi: [10.1111/j.1365-2966.2011.18565.x](https://doi.org/10.1111/j.1365-2966.2011.18565.x)
- Verheijen, M. A. W., & Sancisi, R. 2001, *A&A*, 370, 765, doi: [10.1051/0004-6361:20010090](https://doi.org/10.1051/0004-6361:20010090)
- Wakker, B. P., Hernandez, A. K., French, D. M., et al. 2015, *ApJ*, 814, 40, doi: [10.1088/0004-637X/814/1/40](https://doi.org/10.1088/0004-637X/814/1/40)
- Wakker, B. P., & Savage, B. D. 2009, *ApJS*, 182, 378, doi: [10.1088/0067-0049/182/1/378](https://doi.org/10.1088/0067-0049/182/1/378)
- Yim, K., Wong, T., Xue, R., et al. 2014, *AJ*, 148, 127, doi: [10.1088/0004-6256/148/6/127](https://doi.org/10.1088/0004-6256/148/6/127)

## APPENDIX

## A. SALT GALAXIES

In this section we summarize each galaxy-QSO system observed by SALT. We calculate impact parameters to QSOs and galaxy-absorber velocity separations ( $\Delta v = v_{\text{Ly}\alpha} - v_{\text{sys}}$ ) based on our measured  $v_{\text{sys}}$  values. Here we provide rotation curves and finder chart images for the sub-sample of galaxies with newly observed SALT data. Each rotation curve figure includes a legend with the galaxy name,  $v_{\text{sys}}$ , and  $v_{\text{rot}}$ . Each associated finder chart includes the position of the SALT-RSS slit in red, an arrow toward each nearby QSO with QSO name and impact parameter labels in blue (or a red circle around the QSO for CGCG039-137, the only case where the QSO is within the image), and a physical scale legend in the lower left corner.

## A.1. CGCG039-137

CGCG039-137 is an isolated Scd type galaxy with a measured systemic velocity  $v_{\text{sys}} = 6918 \pm 24 \text{ km s}^{-1}$  and inclination of  $i = 72^\circ$ . The QSO RX\_J1121.2+0326 is located nearby at an impact parameter of 99 kpc and azimuth angle of  $71^\circ$  on the receding side. The data for RX\_J1121.2+0326 has low signal-to-noise ( $\sim 4.2$ ), but we are able to detect Ly $\alpha$  at  $6975 \text{ km s}^{-1}$ , which, at  $\Delta v = 57 \text{ km s}^{-1}$ , lies well within the range of projected velocities consistent with co-rotation (cylindrical model =  $[-36, 137]$ , NFW =  $[-37, 164] \text{ km s}^{-1}$ ).

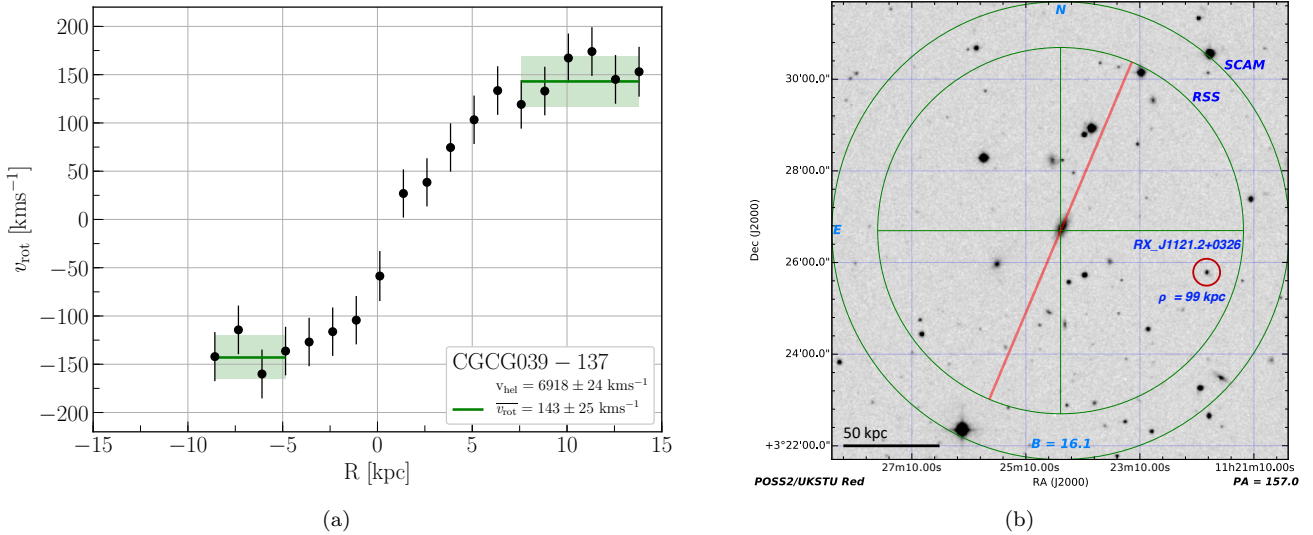


**Figure 9.** a) Rotation curve of CGCG039-137. The solid green line indicates the weighted mean velocity over the corresponding x-axis region, and the shaded green indicates the  $1\sigma$  error in the mean. b) SALT finder chart for CGCG039-137 showing the position of the slit in red.

## A.2. ESO343-G014

ESO343-G014 is an edge-on ( $i = 90^\circ$ ) spiral galaxy with a measured systemic velocity  $v_{\text{sys}} = 9139 \pm 32 \text{ km s}^{-1}$ . It has a smaller neighboring galaxy, 2MASXJ21372816-3824412, located north of its major axis at a projected distance of 216 kpc and velocity of  $9129 \text{ km s}^{-1}$ . The nearest sightline is towards RBS1768 at  $\rho = 466 \text{ kpc}$  and  $74^\circ$  azimuth angle on the approaching side. We detect 3 blended Ly $\alpha$  absorption components toward RBS1768 at  $v_{\text{Ly}\alpha} = 9308, 9360, 9434 \text{ km s}^{-1}$  ( $\Delta v = 169, 221, 295 \text{ km s}^{-1}$ ). This system is highly blended with galactic S II, and therefore their widths are not reliable. All of these are anti-aligned with the rotation of ESO343-G014 relative to the models (cylindrical =  $[-203, 10]$ , NFW =  $[-122, 31] \text{ km s}^{-1}$ ). Unfortunately the presence of 2MASXJ21372816-3824412 makes it difficult to attribute this gas uniquely to ESO343-G014. Additionally, this gas could be attributed to either the approaching or receding side of the disk due to the large impact parameter and high azimuth angle of the sightline.

## A.3. IC5325

IC5325 is a mostly face-on ( $i = 25^\circ$ ) SAB(rs)bc type galaxy with a measured systemic velocity  $v_{\text{sys}} = 1512 \pm 8 \text{ km s}^{-1}$ . Its inclination is just high enough to obtain a reasonable rotation curve. The closest neighboring galaxy

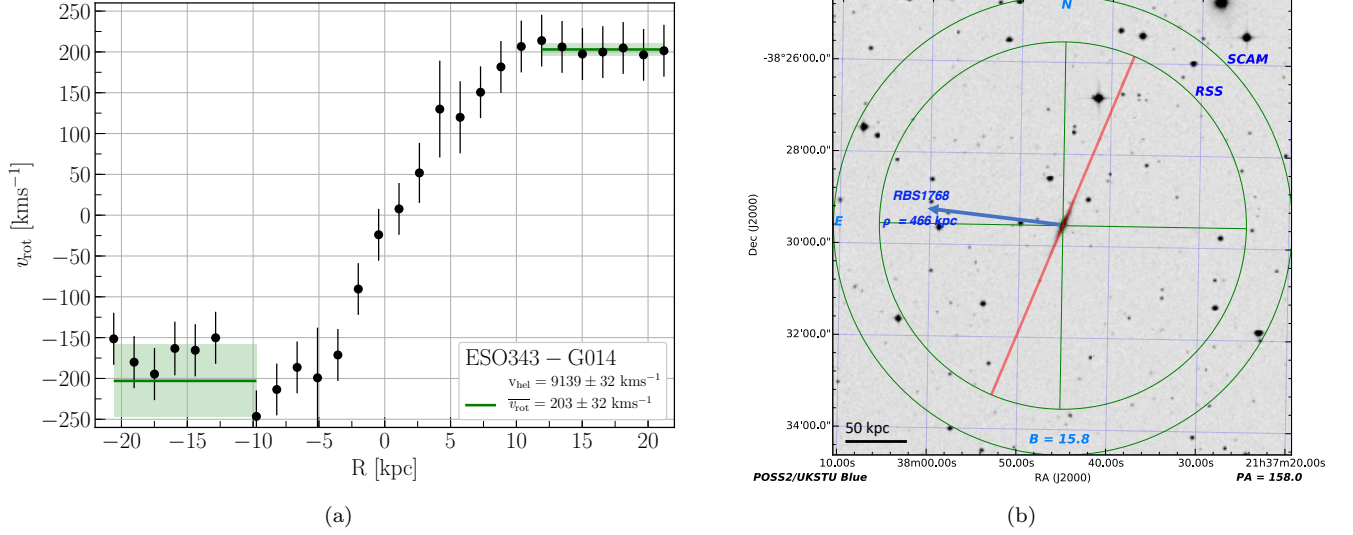


**Figure 10.** a) Rotation curve of ESO343-G014. The solid green line indicates the weighted mean velocity over the corresponding x-axis region, and the shaded green indicates the  $1\sigma$  error in the mean. b) SALT finder chart for ESO343-G014 showing the position of the slit in red.

is ESO347-G020 to the southeast at 306 kpc and  $v_{sys} = 1745 \text{ km s}^{-1}$ . Three other much smaller galaxies are also located  $\sim 450$  kpc to the southwest. The background QSO RBS2000 is located northeast at  $\rho = 314$  kpc and  $64^\circ$  azimuth angle on the approaching side of IC5325. We detect  $\text{Ly}\alpha$  at  $v_{\text{Ly}\alpha} = 1598 \text{ km s}^{-1}$  ( $\Delta v = 86 \text{ km s}^{-1}$ ) towards RBS2000. While this velocity is anti-aligned with the rotation the disk gas relative to our model predictions (cylindrical =  $[-41, -20]$ , NFW =  $[-29, 1] \text{ km s}^{-1}$ ), the low inclination angle of IC5325 leads to a highly uncertain position angle. Without additional observations, we cannot say for certain if the location of RBS2000 actually lies on the approaching or receding side. This position angle uncertainty also means our SALT rotation curve is a lower limit on the true rotation velocity of IC5325.

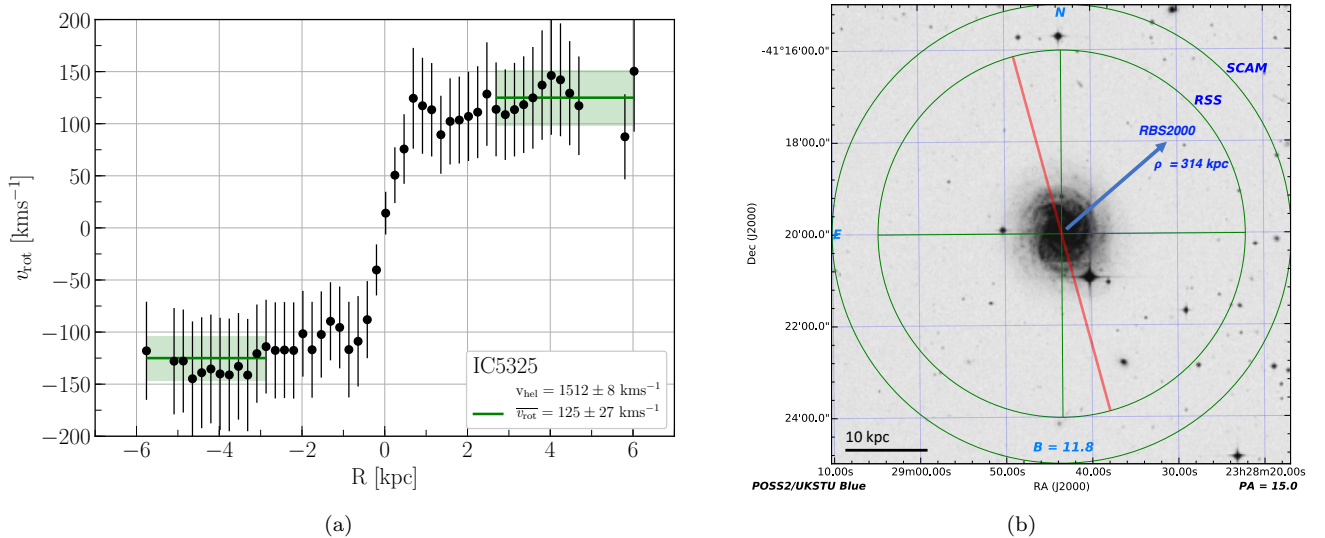


**Figure 11.** a) Rotation curve of IC5325. The solid green line indicates the weighted mean velocity over the corresponding x-axis region, and the shaded green indicates the  $1\sigma$  error in the mean. b) SALT finder chart for IC5325 showing the position of the slit in red.

A.4. *MCG-03-58-009*

MCG-03-58-009 is a massive and very isolated Sc type galaxy at a measured systemic velocity of  $v_{\text{sys}} = 9015 \pm 19 \text{ km s}^{-1}$  and inclination angle of  $i = 61^\circ$ . The background QSO MRC2251-178 is located southeast at  $\rho = 355 \text{ kpc}$  at an azimuth angle of  $71^\circ$  on the receding side. We detect a weak  $\text{Ly}\alpha$  absorber at  $v_{\text{Ly}\alpha} = 9029 \text{ km s}^{-1}$  ( $\Delta v = 14 \text{ km s}^{-1}$ ) towards MRC2251-178. This absorber velocity falls well within the expected range for co-rotation relative to our models (cylindrical =  $[-26, 137]$ , NFW =  $[-42, 83] \text{ km s}^{-1}$ ). Although this absorber matches the velocity expected for co-rotation, the velocity difference ( $\Delta v = 14 \text{ km s}^{-1}$ ) is also within the systemic velocity uncertainty for MCG-03-58-009. The relative weakness of this absorber ( $\text{EW} = 62 \pm 4 \text{ m}\text{\AA}$ ) is somewhat unusual given it's proximity (just outside of  $1 R_{\text{vir}}$ ) to a massive galaxy. If this is representative of an isolated system such as MCG-03-58-009, then we should expect the halo rotational velocity to approach systemic by  $1 R_{\text{vir}}$ .

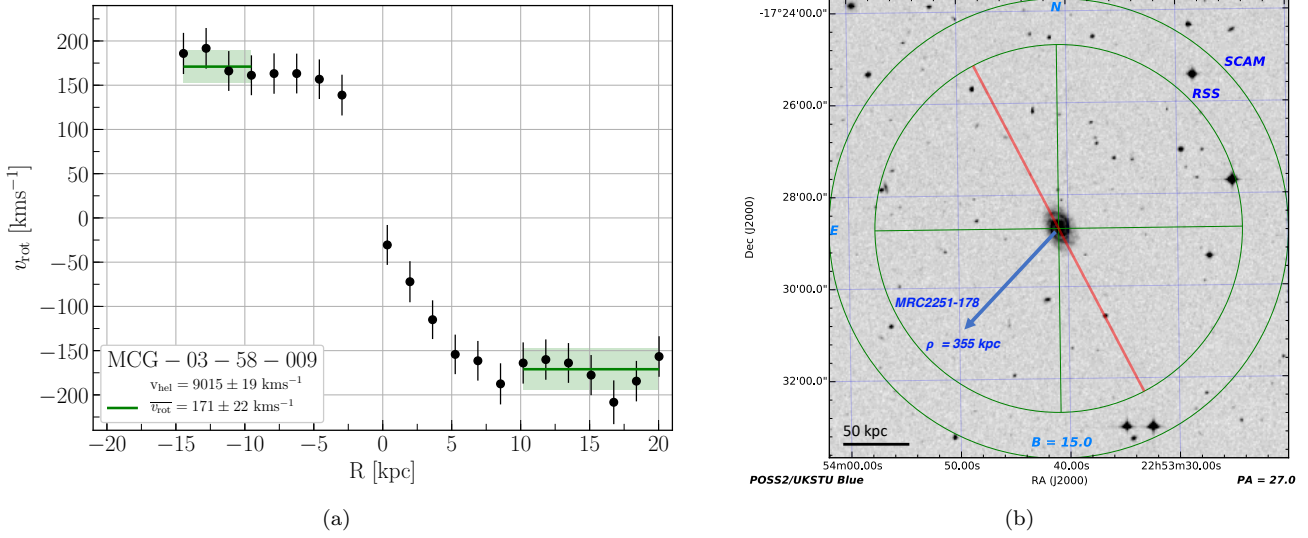


**Figure 12.** a) Rotation curve of MCG-03-58-009. The solid green line indicates the weighted mean velocity over the corresponding x-axis region, and the shaded green indicates the  $1\sigma$  error in the mean. b) SALT finder chart for MCG-03-58-009 showing the position of the slit in red.

A.5. *NGC3633*

NGC3633 is an isolated, edge-on ( $i = 72^\circ$ ) SAa type galaxy with a measured systemic velocity  $v_{\text{sys}} = 2587 \pm 7 \text{ km s}^{-1}$ . Several locations along the disk of NGC3633 show two velocities for emission. We have combined these into a single velocity measurement via a weighted average.

The background QSO RX\_J1121.2+0326 is located southeast at  $\rho = 184 \text{ kpc}$  and  $58^\circ$  azimuth on the approaching side of NGC3633. We detect  $\text{Ly}\alpha$  at  $v_{\text{Ly}\alpha} = 2605 \text{ km s}^{-1}$  ( $\Delta v = 18 \text{ km s}^{-1}$ ) toward RX\_J1121.2+0326. While close to  $v_{\text{sys}}$ , this absorber velocity is just outside our predicted model velocities (cylindrical =  $[-153, -14]$ , NFW =  $[-77, 10] \text{ km s}^{-1}$ ). However, this absorber is also very weak and broad, making the velocity center uncertain by at least  $\sim 10 \text{ km s}^{-1}$ . Taking this along with the uncertainty in  $V_{\text{sys}}$ , this absorber could still be consistent with co-rotation.

A.6. *NGC4939*

NGC4939 is a large SA(s)bc type galaxy with measured systemic velocity  $v_{\text{sys}} = 3093 \pm 33 \text{ km s}^{-1}$  and inclination  $i = 61^\circ$ . The background QSO PG1302-102 is located southeast at  $\rho = 254 \text{ kpc}$  and  $61^\circ$  azimuth angle on the approaching side of NGC4939. We detect a  $\text{Ly}\alpha$  absorber at  $v_{\text{Ly}\alpha} = 3448 \text{ km s}^{-1}$  ( $\Delta v = 355 \text{ km s}^{-1}$ ) towards PG1302-102. As this absorber is located on the approaching side, we can easily rule out co-rotation in this case. NGC4939 does not have any close neighbors, so represents an intriguing case against co-rotation for gas past  $1 R_{\text{vir}}$ .

A.7. *NGC5786*

NGC5786 is a large, strongly-barred spiral galaxy with measured systemic velocity  $v_{\text{sys}} = 2975 \pm 22 \text{ km s}^{-1}$  and inclination  $i = 65^\circ$ . The background QSO QSO1500-4140 is located directly east at  $\rho = 453 \text{ kpc}$  and  $1^\circ$  azimuth angle on the receding side of NGC5786. We detect  $\text{Ly}\alpha$  at  $v_{\text{Ly}\alpha} = 3138 \text{ km s}^{-1}$  ( $\Delta v = 163 \text{ km s}^{-1}$ ) toward QSO1500-4140,



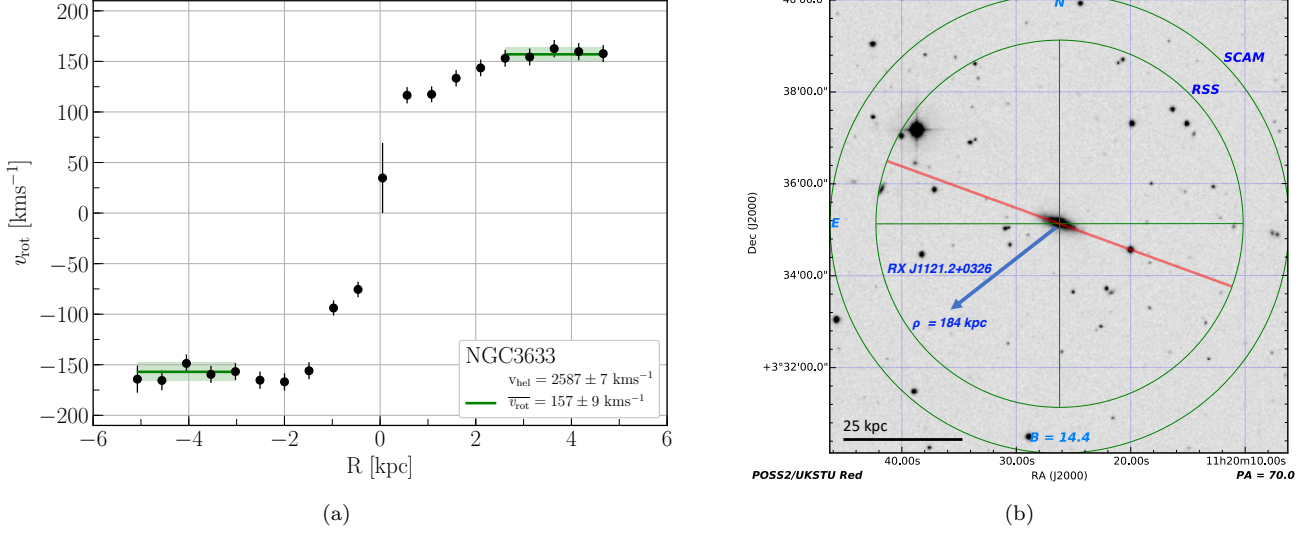


**Figure 13.** a) Rotation curve of NGC3633. The solid green line indicates the weighted mean velocity over the corresponding x-axis region, and the shaded green indicates the  $1\sigma$  error in the mean. b) SALT finder chart for NGC3633 showing the position of the slit in red.

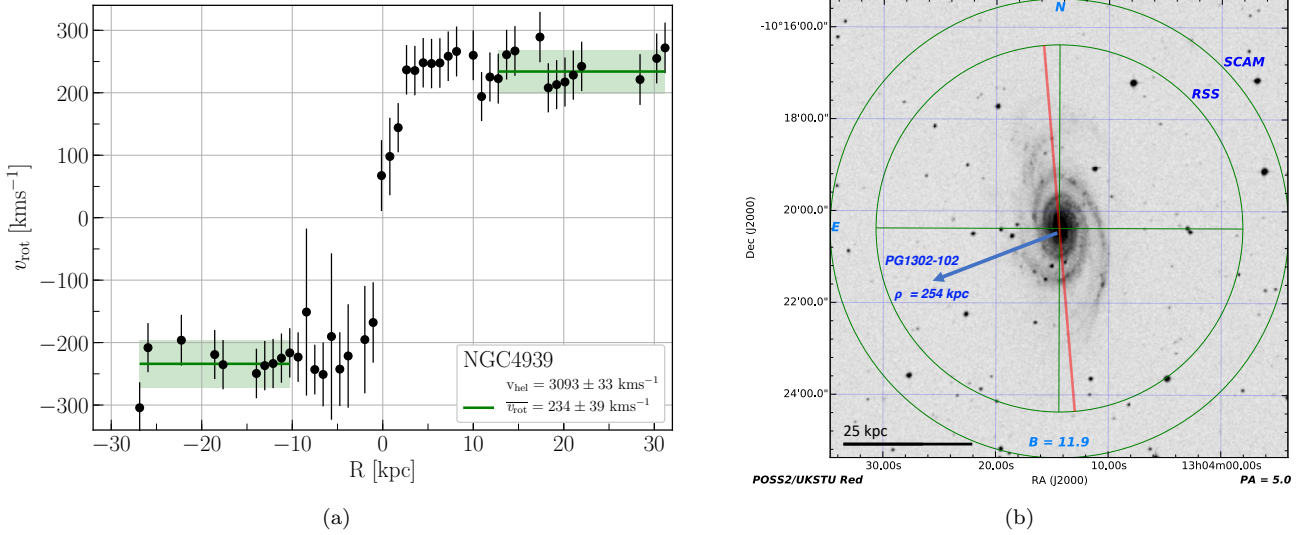


**Figure 14.** a) Rotation curve of NGC4939. The solid green line indicates the weighted mean velocity over the corresponding x-axis region, and the shaded green indicates the  $1\sigma$  error in the mean. b) SALT finder chart for NGC4939 showing the position of the slit in red.

which is slightly above the model predicted velocity range (cylindrical =  $[106, 160]$ , NFW =  $[19, 67]$   $\text{km s}^{-1}$ ). However, the two neighboring galaxies ESO327-G038 and ESO327-G039 are both located south of NGC5786 at  $\rho = 62, 296$  kpc, respectively. These nearby galaxies, along with the large distance to the absorption ( $\sim 2.5R_{\text{vir}}$ ), make it difficult to believe there is a connection to a NGC5786 extended disk.

#### A.8. UGC09760

UGC09760 is an edge-on ( $i = 90^\circ$ ), slow-rotating Sd galaxy with measured systemic velocity  $v_{\text{sys}} = 2094 \pm 16$   $\text{km s}^{-1}$ . This systemic velocity deviates slightly from other published redshifts, such as the The Updated Zwicky Catalog value of  $v_{\text{sys}} = 2023 \pm 2$   $\text{km s}^{-1}$  (Falco et al. 1999). This is likely due to our method of imposing rotation symmetry and averaging the approaching and receding velocities to derive  $v_{\text{sys}}$ . If we do not sample the rotation curve far enough out, a systematic offset is not unreasonable. Indeed, we do not detect the rotation curve turnover or flattening point.

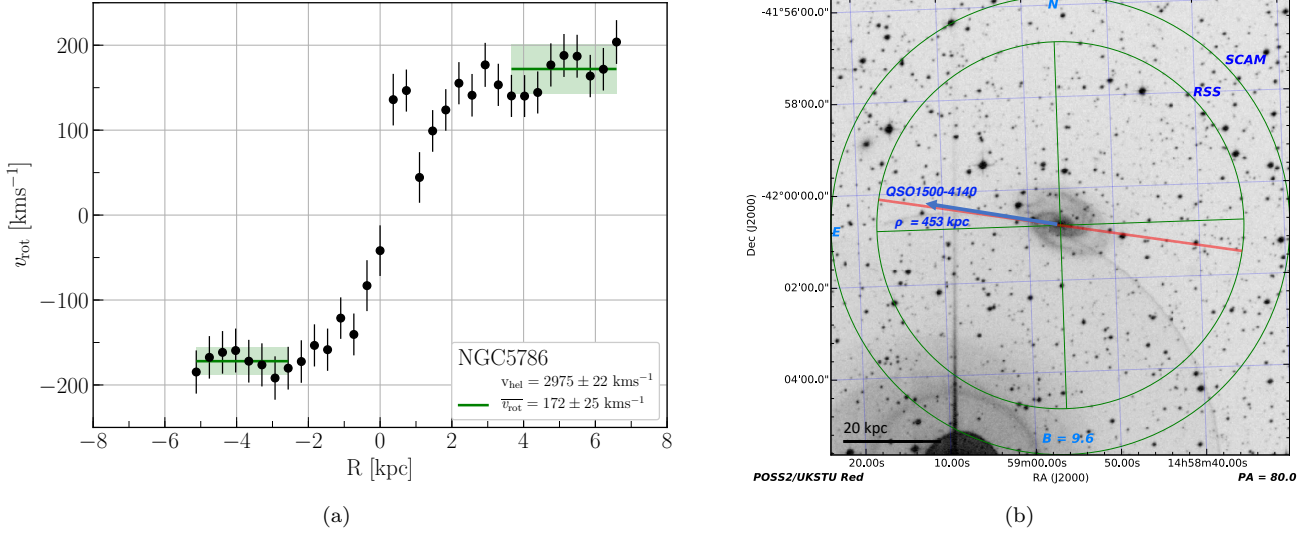


**Figure 15.** a) Rotation curve of NGC5786. The solid green line indicates the weighted mean velocity over the corresponding x-axis region, and the shaded green indicates the  $1\sigma$  error in the mean. b) SALT finder chart for NGC5786 showing the position of the slit in red.

The background QSO SDSSJ151237.15+012846.0 is located southeast at  $\rho = 123$  kpc and  $90^\circ$  azimuth angle. We detect  $\text{Ly}\alpha$  absorption at  $v_{\text{Ly}\alpha} = 2029 \text{ km s}^{-1}$  ( $\Delta v = -65 \text{ km s}^{-1}$ ) toward SDSSJ151237.15+012846.0. This velocity falls outside the model predictions for co-rotation (cylindrical =  $[-30, 30]$ , NFW =  $[-30, 86] \text{ km s}^{-1}$ ), but unfortunately this sightline lies almost exactly at an azimuth of  $90^\circ$ . Hence, the motion of this gas could easily be either co-rotating or counter-rotating depending on a minute change in the position angle assigned to UGC09760. This is especially true if we assume our measured  $v_{\text{sys}}$  is erroneously high, and indeed closer to the values obtained by other observations. For example, if we adjust the position angle by a single degree, to  $56^\circ$  instead of  $57^\circ$ , our model predictions become (cylindrical =  $[-30, 30]$ , NFW =  $[-79, 30] \text{ km s}^{-1}$ ) and this absorber becomes consistent with co-rotation in the NFW model.

It is worth noting that there are several small satellite galaxies nearby, including SDSSJ151208.16+013508.5, SDSSJ151121.63+013637.6, SDSSJ151241.38+013723.7 and UGC09746 (impact parameters  $\rho = 53, 88, 82, 230$  kpc respectively). All of these galaxies lie slightly blue-ward of UGC09760, and thus *farther* away in velocity from the  $\text{Ly}\alpha$  absorber at  $2029 \text{ km s}^{-1}$ .

## B. ANCILLARY DATA

To increase our sample size we have also searched the literature for galaxies with published rotation curves and orientations. Unfortunately, while the rotation velocity is available for thousands of galaxies, only a handful of publications also include the *orientation* of the rotation on the sky. Of these, we were able to find 18 additional galaxies which have a systemic velocity greater than  $\sim 500 \text{ km s}^{-1}$ , and are near to a COS or STIS sightline with available data. We have included 3 of the galaxy-QSO systems analyzed by Côté et al. (2005). We briefly summarize each of these systems here (see Sections B.13 - B.8), and refer the reader to Côté et al. (2005) for a more complete discussion. As new spectra and redshift-independent distances are available for these systems our results, while similar, are not identical.

### B.1. NGC2770

NGC2770 is a large, edge-on ( $i = 80^\circ$ ) Sc type galaxy with systemic velocity  $v_{\text{sys}} = 1948 \pm 2 \text{ km s}^{-1}$ . It is mostly isolated except for two nearby small dwarfs MCG+06-20-036NED02 and GALEXASCJ090946.88+330840.4 (both 25 kpc away, on opposite sides of NGC2770). We take the rotation curve and orientation information produced by Rhee & van Albada (1996). There are five nearby QSOs, which we present in order of increasing impact parameter.

First, the QSO FBQSJ0908+3246 is located south at  $\rho = 204$  kpc and  $59^\circ$  azimuth angle on the approaching side of NGC2770. We detect  $\text{Ly}\alpha$  at  $v_{\text{Ly}\alpha} = 1915, 1982 \text{ km s}^{-1}$  ( $\Delta v = -33, 34 \text{ km s}^{-1}$ ). Relative to our model predictions (cylindrical =  $[-146, -4]$ , NFW =  $[-117, 10] \text{ km s}^{-1}$ ), only the lower velocity line can be described as co-rotating.

Second, the QSO TON1015 is located northeast at  $\rho = 218$  kpc and  $61^\circ$  azimuth angle on the receding side of NGC2770. We detect  $\text{Ly}\alpha$  at  $v_{\text{Ly}\alpha} = 1833, 1985 \text{ km s}^{-1}$  ( $\Delta v = -115, 37 \text{ km s}^{-1}$ ). Relative to our model predictions (cylindrical =  $[3, 146]$ , NFW =  $[-10, 115] \text{ km s}^{-1}$ ), only the higher velocity absorber can be described as co-rotating.

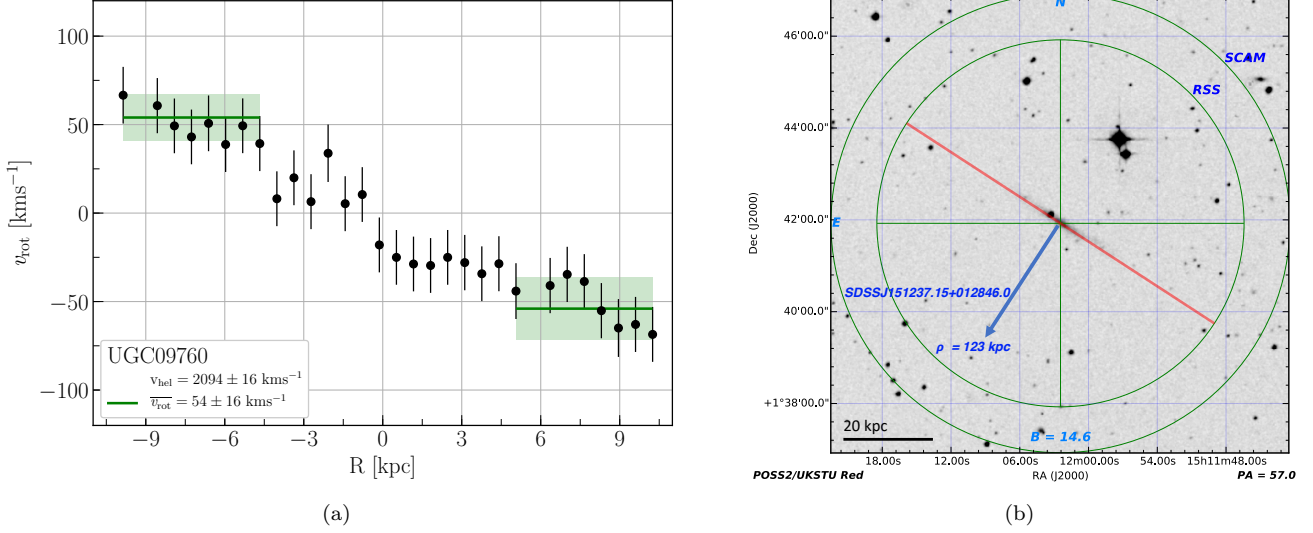


**Figure 16.** a) Rotation curve of UGC09760. The solid green line indicates the weighted mean velocity over the corresponding x-axis region, and the shaded green indicates the  $1\sigma$  error in the mean. b) SALT finder chart for UGC09760 showing the position of the slit in red.

Third the QSO SDSSJ091127.30+325337.0 is located southeast at  $\rho = 234$  kpc and  $30^\circ$  azimuth angle on the approaching side of NGC2770. We detect  $\text{Ly}\alpha$  at  $v_{\text{Ly}\alpha} = 2063 \text{ km s}^{-1}$  ( $\Delta v = 115 \text{ km s}^{-1}$ ). Relative to our model predictions (cylindrical =  $[-150, -43]$ , NFW =  $[-117, -19] \text{ km s}^{-1}$ ), this absorber appears to be counter-rotating.

Fourth, the QSO SDSSJ091052.80+333008.0 is located northeast at  $\rho = 239$  kpc and  $66^\circ$  azimuth angle on the receding side of NGC2770. We detect  $\text{Ly}\alpha$  at  $v_{\text{sys}} = 1824, 1975 \text{ km s}^{-1}$  ( $\Delta v = -124, 27 \text{ km s}^{-1}$ ). Relative to our model predictions (cylindrical =  $[6, 145]$ , NFW =  $[-7, 112] \text{ km s}^{-1}$ ), only the higher velocity absorber can be described as co-rotating.

Finally, the QSO TON1009 is located south at  $\rho = 267$  kpc and  $41^\circ$  azimuth angle on the approaching side of NGC2770. We detect  $\text{Ly}\alpha$  at  $v_{\text{sys}} = 1908, 1980 \text{ km s}^{-1}$  ( $\Delta v = -40, 32 \text{ km s}^{-1}$ ). Relative to our model predictions (cylindrical =  $[-146, -39]$ , NFW =  $[-110, -14] \text{ km s}^{-1}$ ), only the lower velocity absorber can be described as co-rotating.

Interestingly, we appear to be detecting extended gas structures in these 5 sightlines. Toward the northeast we find TON1015 and SDSSJ091052.80+333008.0 and a set of absorber pairs at  $v_{\text{Ly}\alpha} = 1833, 1824 \text{ km s}^{-1}$  and  $v_{\text{Ly}\alpha} = 1985, 1975 \text{ km s}^{-1}$  each having very similar EW and  $N_{\text{HI}}$ , and remarkably similar appearing line-structure. Adopting a distance of 28.6 Mpc to this cloud, we calculate a linear separation between TON1015 and SDSSJ091052.80+333008.0 of 28 kpc. Hence, there appears to be two distinct clouds of at least 28 kpc in physical extent sandwiched around the systemic velocity of NGC2770. Toward the south we find TON1009 and FBQSJ0908+3246 and a set of absorber pairs at  $v_{\text{Ly}\alpha} = 1908, 1915 \text{ km s}^{-1}$  and  $v_{\text{Ly}\alpha} = 1980, 1982 \text{ km s}^{-1}$ , again with similar EW,  $N_{\text{HI}}$  and line-shapes.

## B.2. NGC3067

NGC3067 is a mostly edge-on ( $i = 71^\circ$ ) SAB(s)ab type galaxy with systemic velocity  $v_{\text{sys}} = 1465 \pm 5 \text{ km s}^{-1}$ . This galaxy and the nearby QSO sightline toward 3C232 is a particularly well studied system. They are separated by only  $\rho = 11$  kpc ( $74^\circ$  azimuth angle on the northwest, receding side) and a Lyman Limit System (LLS) with column density  $N_{\text{HI}} = 1 \times 10^{20} \text{ cm}^{-2}$  is detected toward 3C232 at  $v_{\text{Ly}\alpha} = 1408 \text{ km s}^{-1}$ , which has been postulated as a high velocity cloud (HVC) orbiting NGC3067 (Carilli et al. 1989; Keeney et al. 2005).

We obtained the rotation curve for NGC3067 from Rubin et al. (1982) and the orientation from Carilli et al. (1989). We fit a single component to the Lyman Limit System with  $v_{\text{Ly}\alpha} = 1408 \text{ km s}^{-1}$  and  $\log N_{\text{HI}} = 20.086 \text{ cm}^{-2}$ . Some studies suggest this system could have 2 or more components (e.g., Keeney et al. 2005 and Stocke et al. 2010), but we do not see strong evidence for multiple components here.

A second QSO SDSSJ095914.80+320357.0 is located farther away, to the southeast at  $\rho = 128$  kpc and  $43^\circ$  azimuth angle on the receding side of NGC3067. We detect  $\text{Ly}\alpha$  at  $v_{\text{Ly}\alpha} = 1493 \text{ km s}^{-1}$  ( $\Delta v = 28 \text{ km s}^{-1}$ ), which agrees well with our model predicted velocity range (cylindrical =  $[11, 138]$ , NFW =  $[-12, 81] \text{ km s}^{-1}$ ).

## B.3. NGC3198

NGC3198 is a SB(rs)c type galaxy with systemic velocity  $v_{\text{sys}} = 660 \pm 1 \text{ km s}^{-1}$  and inclination  $i = 73^\circ$ . It is a well studied galaxy, and is included in the detailed THINGS rotation curve study of [de Blok et al. \(2008\)](#). NGC3198 has an even and flat rotation curve, with an average velocity of  $v_{\text{rot}} = 152 \text{ km s}^{-1}$ . The background QSO RX\_1017.5+4702 is located northeast at  $\rho = 370 \text{ kpc}$  and  $55^\circ$  azimuth angle on the approaching side of NGC3198. We detect Ly $\alpha$  toward RX\_1017.5+4702 at  $v_{\text{Ly}\alpha} = 629 \text{ km s}^{-1}$  ( $\Delta v = -32 \text{ km s}^{-1}$ ), which can nicely be described by a co-rotating disk based on our model predicted velocity range (cylindrical =  $[-153, -21]$ , NFW =  $[-91, 6] \text{ km s}^{-1}$ ). We note that the small dwarf galaxy SDSSJ101848.77+452137.0 is located 65 kpc away from NGC3198 toward the southwest.

## B.4. NGC3351

NGC3351 is a mostly face-on ( $i = 42^\circ$ ) SB(r)b type galaxy with systemic velocity  $v_{\text{sys}} = 778 \pm 4 \text{ km s}^{-1}$ . It is located  $\sim 200 \text{ kpc}$  southwest of the core of the Leo I group. We take the rotation curve and orientation produced by [Dicaire et al. \(2008\)](#). While we expect any extended disk rotation to be quickly disrupted due to the complex Leo I environment, this galaxy also has one of the closest sightlines in our sample with SDSSJ104335.90+115129.0 at  $\rho = 31 \text{ kpc}$  and  $13^\circ$  azimuth on the northwest, approaching side. We detect Ly $\alpha$  at  $v_{\text{Ly}\alpha} = 717, 882, 1030 \text{ km s}^{-1}$  ( $\Delta v = -61, 104, 252 \text{ km s}^{-1}$ ) toward this sightline. The lowest velocity absorber agrees nicely with both models for co-rotation, while the other two are above our model predictions (cylindrical =  $[-99, 12]$ , NFW =  $[-68, 20] \text{ km s}^{-1}$ ). We also detect multiple metal ions associated with the  $v_{\text{Ly}\alpha} = 717 \text{ km s}^{-1}$  line, including C II, N I, N V, O I, Si II, Si III, Si IV, S II, and Fe II.

## B.5. NGC3432

NGC3432 is an edge-on ( $i = 90^\circ$ ) SB(s)m type galaxy with systemic velocity  $v_{\text{sys}} = 616 \pm 4 \text{ km s}^{-1}$ . It is interacting with the nearby dwarf galaxy UGC05983 located 11 kpc away and at  $v_{\text{sys}} = 765 \text{ km s}^{-1}$ . We take a rotation curve and orientation for NGC3432 from [Rhee & van Albada \(1996\)](#). The QSO CSO295 is located just 20 kpc away and just to the receding side of the minor axis ( $82^\circ$  azimuth angle). This is the second closest pair in our sample, after the 11 kpc separated NGC3067-3C232 system. We detect Ly $\alpha$  at  $v_{\text{Ly}\alpha} = 600, 662 \text{ km s}^{-1}$  ( $\Delta v = -16, 46 \text{ km s}^{-1}$ ) toward CSO295. Relative to our model predictions (cylindrical =  $[-37, 48]$ , NFW =  $[-37, 134] \text{ km s}^{-1}$ ) both of these absorbers are consistent with co-rotation. In fact, this orientation would represent the lower-velocity cloud existing toward the near-edge of the halo and the higher velocity cloud lying very close to the plane of the stellar disk. We also detect C II, Si II, Si III, and Si IV associated with this absorption system.

A second QSO RX\_J1054.2+3511 is located south at  $\rho = 290 \text{ kpc}$  and  $57^\circ$  azimuth angle on the receding side of NGC3432. We detect Ly $\alpha$  at  $v_{\text{sys}} = 703 \text{ km s}^{-1}$  ( $\Delta v = 87 \text{ km s}^{-1}$ ) toward RX\_J1054.2+3511. Relative to our model predictions (cylindrical =  $[0, 123]$ , NFW =  $[-9, 111] \text{ km s}^{-1}$ ), this absorber is consistent with co-rotation as well.

## B.6. NGC3631

NGC3631 is a mostly face-on ( $i = 17^\circ$ ) SA(s)c type galaxy with systemic velocity  $v_{\text{sys}} = 1156 \pm 1 \text{ km s}^{-1}$ . We take the rotation curve and orientation information produced by [Knapen \(1997\)](#). There are 4 nearby QSOs, which we will present in order of increasing impact parameter.

First, the closest background QSO RX\_J1117.6+5301 is located southwest at  $\rho = 78 \text{ kpc}$  and  $75^\circ$  azimuth angle on the receding side of NGC3631. We detect Ly $\alpha$  at  $v_{\text{Ly}\alpha} = 1131, 1259 \text{ km s}^{-1}$  ( $\Delta v = -25, 103 \text{ km s}^{-1}$ ). Both of these lines fall outside of our model predicted velocities (cylindrical =  $[10, 24]$ , NFW =  $[1, 21] \text{ km s}^{-1}$ ).

Second, background QSO SDSSJ112448.30+531818.0 is located northeast at  $\rho = 86 \text{ kpc}$  and  $74^\circ$  azimuth angle on the approaching side of NGC3631. We detect Ly $\alpha$  at  $v_{\text{Ly}\alpha} = 1019, 1141 \text{ km s}^{-1}$  ( $\Delta v = -137, -15 \text{ km s}^{-1}$ ). Only the higher velocity absorber falls within our model predicted velocity range (cylindrical =  $[-26, -11]$ , NFW =  $[-22, 1] \text{ km s}^{-1}$ ).

Third, the background QSO SDSSJ111443.70+525834.0 is located in the same direction but farther than RX\_J1117.6+5301, at  $\rho = 145 \text{ kpc}$  and  $72^\circ$  azimuth angle on the receding side of NGC3631. We detect Ly $\alpha$  at  $v_{\text{Ly}\alpha} = 1163 \text{ km s}^{-1}$  ( $\Delta v = 7 \text{ km s}^{-1}$ ). This absorber appears to agree well with our model predicted velocity range (cylindrical =  $[8, 29]$ , NFW =  $[-5, 24] \text{ km s}^{-1}$ ).

Finally, the background QSO SBS1116+523 is located south at  $\rho = 163 \text{ kpc}$  and  $40^\circ$  azimuth angle on the approaching side of NGC3631, but we do not detect any Ly $\alpha$  within  $\pm 400$  of NGC3631.

## B.7. NGC3666

NGC3666 is a mostly isolated and edge-on ( $i = 78^\circ$ ) SA(rs)c type galaxy with systemic velocity  $v_{\text{sys}} = 1060 \pm 1 \text{ km s}^{-1}$ . We take the rotation curve and orientation information produced by [Rhee & van Albada \(1996\)](#). The QSO SDSSJ112439.50+113117.0 is located north at  $\rho = 58 \text{ kpc}$  and  $83^\circ$  azimuth angle on the approaching side of NGC3666. We detect Ly $\alpha$  at  $v_{\text{sys}} = 1047, 1099 \text{ km s}^{-1}$  ( $\Delta v = -13, 39 \text{ km s}^{-1}$ ) toward SDSSJ112439.50+113117.0. Relative to our



model predictions (cylindrical =  $[-87, 20]$ , NFW =  $[-136, 20]$   $\text{km s}^{-1}$ ) the lower velocity absorber is consistent with co-rotation, while the other is slightly too high in velocity.

#### B.8. UGC04238

UGC04238 is an isolated, mostly edge-on ( $i = 62^\circ$ ) SBd type galaxy with systemic velocity  $v_{\text{sys}} = 1544 \pm 7 \text{ km s}^{-1}$ . We take the rotation curve and orientation information produced by Côté et al. (2005). The background QSO PG0804+761 is located directly south at  $\rho = 148 \text{ kpc}$  and  $59^\circ$  azimuth on the receding side of UGC04238. We detect Ly $\alpha$  at  $v_{\text{Ly}\alpha} = 1526, 1593 \text{ km s}^{-1}$  ( $\Delta v = -18, 49 \text{ km s}^{-1}$ ) toward PG0804+761. Relative to our model predictions (cylindrical =  $[-3, 86]$ , NFW =  $[-10, 75]$   $\text{km s}^{-1}$ ), although both are close, only the absorber at  $1593 \text{ km s}^{-1}$  (the lower EW of the two) falls within the expected velocity range for co-rotation.

#### B.9. NGC4529

NGC4529 is an edge-on ( $i = 80^\circ$ ) and isolated Scd type galaxy with systemic velocity  $v_{\text{sys}} = 2536 \pm 11 \text{ km s}^{-1}$ . We take the rotation curve and orientation information produced by Côté et al. (2005). The QSO MRK771 is located west at  $\rho = 159 \text{ kpc}$  and  $23^\circ$  azimuth angle on the approaching side of NGC4529. We detect Ly $\alpha$  at  $v_{\text{Ly}\alpha} = 2553 \text{ km s}^{-1}$  ( $\Delta v = 17 \text{ km s}^{-1}$ ), which is anti-rotating relative to our model predictions (cylindrical =  $[-103, -40]$ , NFW =  $[-87, -25]$   $\text{km s}^{-1}$ ). As Côté et al. (2005) conclude, “there is simply no physical way to produce such a velocity with an extending co-rotating disk.”

#### B.10. NGC4565

NGC4565 is an edge-on ( $i = 86^\circ$ ) SA(s)b type galaxy with systemic velocity  $v_{\text{sys}} = 1230 \pm 5 \text{ km s}^{-1}$ . We take the rotation curve and orientation produced by Sofue (1996). The background QSO RX\_J1236.0+2641 is located directly north at  $\rho = 147 \text{ kpc}$  and  $41^\circ$  azimuth angle on receding side of NGC4565. We detect Ly $\alpha$  absorption at  $v_{\text{Ly}\alpha} = 1009, 1166, 1254 \text{ km s}^{-1}$  ( $\Delta v = -221, -64, 24 \text{ km s}^{-1}$ ) toward RX\_J1236.0+2641. Only the  $v_{\text{Ly}\alpha} = 1254 \text{ km s}^{-1}$  line is consistent with co-rotating gas relative to our model predictions (cylindrical =  $[-2, 246]$ , NFW =  $[-30, 144]$   $\text{km s}^{-1}$ ). However, the presence of several other nearby galaxies (e.g., NGC4559, NGC4562) surely disrupts any possible extended disk rotation that would otherwise be detectable via sightline absorption.

#### B.11. NGC5907

NGC5907 is a large, edge-on ( $i = 90^\circ$ ) SA(s)c type galaxy with systemic velocity  $v_{\text{sys}} = 667 \pm 3 \text{ km s}^{-1}$ . We take the rotation curve and orientation produced by Yim et al. (2014). The background QSO SBS1503+570 is located northwest at  $\rho = 413 \text{ kpc}$  and  $47^\circ$  azimuth angle on the receding side of NGC5907. We detect Ly $\alpha$  at  $v_{\text{Ly}\alpha} = 708 \text{ km s}^{-1}$  ( $\Delta v = 38 \text{ km s}^{-1}$ ), which falls within the model predictions for co-rotation (cylindrical =  $[31, 228]$ , NFW =  $[-24, 101]$   $\text{km s}^{-1}$ ). Unfortunately there are several other nearby galaxies, the largest of which being NGC5866 (diameter  $D = 20.8$  and impact parameter  $\rho = 208 \text{ kpc}$ , versus for NGC5907 -  $D = 50.6$  and  $\rho = 413 \text{ kpc}$ ). Hence, it is difficult to assign this absorber to NGC5907 alone.

#### B.12. NGC5951

NGC5951 is a large, edge-on ( $i = 74^\circ$ ) SBc type galaxy with systemic velocity  $v_{\text{sys}} = 1780 \pm 1 \text{ km s}^{-1}$ . We take the rotation curve and orientation for NGC5951 from Rhee & van Albada (1996). The QSO 2E1530+1511 is located east at  $\rho = 55 \text{ kpc}$  and  $85^\circ$  azimuth angle on the receding side of NGC5951. We detect Ly $\alpha$  at  $v_{\text{Ly}\alpha} = 1795, 1953 \text{ km s}^{-1}$  ( $\Delta v = 15, 173 \text{ km s}^{-1}$ ) toward 2E1530+1511. Relative to our model predictions (cylindrical =  $[-31, 114]$ , NFW =  $[-32, 125]$   $\text{km s}^{-1}$ ), the lower velocity absorber is consistent with co-rotation while the other is a bit outside of the upper range. The pair of galaxies NGC5954 and NGC5953 are nearby ( $\sim 100 \text{ kpc}$ ), but the sightline toward 2E1530+1511 is closer and on the opposite side of NGC5951. Given the systemic velocity for the nearby galaxies NGC5954 and NGC5953 ( $v_{\text{sys}} = 1959, 1965 \text{ km s}^{-1}$ ), this absorber is likely also linked with that system.

#### B.13. NGC6140

NGC6140 is a small SB(s)cd type galaxy with systemic velocity  $v_{\text{sys}} = 910 \pm 4 \text{ km s}^{-1}$  and inclination  $i = 49^\circ$ . We take the rotation curve and orientation information produced by Côté et al. (2005). A background QSO Mrk876 is located northwest at  $\rho = 113 \text{ kpc}$  and azimuth angle  $21^\circ$  (although this is somewhat uncertain; the position angle for NGC6140 could be closer to  $60^\circ$  than our adopted value of  $94^\circ$  due to it being mostly face on, faint, and strongly barred). We detect Ly $\alpha$  at  $v_{\text{Ly}\alpha} = 939 \text{ km s}^{-1}$  ( $\Delta v = 29 \text{ km s}^{-1}$ ) toward Mrk876. This absorber velocity is of the correct *sign*, but just under the the model predicted velocity range (cylindrical =  $[40, 101]$ , NFW =  $[35, 102]$   $\text{km s}^{-1}$ ) for co-rotation. However, this absorber is still likely co-rotating given both the velocity and position angle uncertainties. Additionally, we detect Ly $\beta$  and O VI associated with this Ly $\alpha$  absorber (see Narayanan et al. 2010).

B.14. *UGC06446*

UGC06446 is a Sd type galaxy with systemic velocity  $v_{\text{sys}} = 645 \pm 1 \text{ km s}^{-1}$  and inclination  $i = 52^\circ$  on the far northwest edge of the Ursa Major cluster of galaxies. We take the rotation curve and orientation information produced by Verheijen & Sancisi (2001) and Swaters et al. (2009). The background QSO SDSSJ112448.30+531818.0 is located southwest at  $\rho = 143 \text{ kpc}$  and  $22^\circ$  azimuth angle on the receding side of UGC06446. We detect  $\text{Ly}\alpha$  at  $v_{\text{Ly}\alpha} = 664, 1019 \text{ km s}^{-1}$  ( $\Delta v = 20, 375 \text{ km s}^{-1}$ ). The absorber at  $v_{\text{Ly}\alpha} = 664$  falls well within our model predicted co-rotation range (cylindrical =  $[-9, 65]$ , NFW =  $[-15, 61] \text{ km s}^{-1}$ ), but the absorber at  $v_{\text{Ly}\alpha} = 1019$  is far more likely to be associated with NGC3631 ( $\rho = 86 \text{ kpc}$ ,  $v_{\text{sys}} = 1156 \text{ km s}^{-1}$ ). We therefore treat these as separate systems.

B.15. *NGC7817*

NGC7817 is an edge-on ( $i = 80^\circ$ ) SAbc type galaxy with systemic velocity  $v_{\text{sys}} = 2309 \pm 4 \text{ km s}^{-1}$ . We take the rotation curve and orientation information produced by Rhee & van Albada (1996). The background QSO MRK335 is located southeast at  $\rho = 343 \text{ kpc}$  and almost directly along the minor axis of NGC7817 ( $90^\circ$  azimuth angle). We detect  $\text{Ly}\alpha$  at  $v_{\text{sys}} = 1954, 2274 \text{ km s}^{-1}$  ( $\Delta v = -355, -35 \text{ km s}^{-1}$ ) toward MRK335. Because these absorbers lie almost exactly along the minor axis, our model predicts a very narrow velocity range for co-rotation (cylindrical =  $[-26, -24]$ , NFW =  $[-26, -24] \text{ km s}^{-1}$ ). While the higher velocity line falls a mere  $9 \text{ km s}^{-1}$  outside this predicted range, the absorption at  $1954 \text{ km s}^{-1}$  is likely not directly associated with NGC7817 given the large velocity difference. Additionally, the neighboring dwarf galaxy ESDOF538-02 ( $v_{\text{sys}} = 2175 \text{ km s}^{-1}$ ) appears in the same direction as MRK335 and only  $\rho = 57 \text{ kpc}$  away from NGC7817, and NSA126180 ( $v_{\text{sys}} = 1950 \text{ km s}^{-1}$ ) appears only  $\rho = 83 \text{ kpc}$  away from MRK335.

B.16. *UGC08146*

UGC08146 is an isolated and edge-on ( $i = 78^\circ$ ) Sd type galaxy with systemic velocity  $v_{\text{sys}} = 670 \pm 1 \text{ km s}^{-1}$ . This galaxy (and the nearby QSO PG1259+593) are included in the Côté et al. (2005) sample also, but we have taken the rotation curve and orientation information from Rhee & van Albada (1996). The QSO PG1259+593 is located northwest at  $\rho = 114 \text{ kpc}$  at  $50^\circ$  azimuth angle on the receding side of UGC08146. While Côté et al. (2005) cite a single  $\text{Ly}\alpha$  component at  $v_{\text{Ly}\alpha} = 679 \text{ km s}^{-1}$ , we detect two components at  $v_{\text{Ly}\alpha} = 646, 683 \text{ km s}^{-1}$  ( $\Delta v = -24, 13 \text{ km s}^{-1}$ ), in the higher signal-to-noise COS data now available for PG1259+593. Relative to our model predictions (cylindrical =  $[-13, 82]$ , NFW =  $[-16, 83] \text{ km s}^{-1}$ ), the higher velocity component is consistent with co-rotation, and the other component is only  $8 \text{ km s}^{-1}$  shy of falling into the NFW co-rotation range as well.